OXFORD UNIVERSITY PRESS | Publications of the Astronomical Society of Japan

The role of hierarchy in Galactic molecular clouds

Journal:	*Publications of the Astronomical Society of Japan*
Manuscript ID	Draft
Manuscript Type:	Paper
Date Submitted by the Author:	n/a
Complete List of Authors:	Sasaki, Kotora; University of Tsukuba, Graduate School of Science and Technology Kuno, Nario; University of Tsukuba, Fukushima, Hajime; University of Tsukuba, Nozaki, Shingo; Kyushu University Faculty of Sciences Graduate School of Sciences Department of Earth and Planetary Sciences
Keywords:	stars: formation, stars: massive, ISM: clouds, ISM: kineatics and dynamics, ISM: structure

Publications of the Astronomical Society of Japan, 2026, **00**, 1–18
doi: 10.1093/pasj/xxx000
Advance access publication date:

The role of hierarchy in Galactic molecular clouds

Kotora SASAKI,[1,*] Nario KUNO,[2] Hajime FUKUSHIMA,[3] and Shingo NOZAKI[4]

[1]Doctoral Program in Physics, Degree Programs in Pure and Applied Sciences, Graduate School of Science and Technology, University of Tsukuba, 1-1-1 Tennodai, Tsukuba, Ibaraki 305-8577, Japan
[2]Department of Physics, Graduate School of Pure and Applied Sciences, University of Tsukuba, 1-1-1 Tennodai, Tsukuba, Ibaraki 305-8577, Japan
[3]Center for Computational Sciences, University of Tsukuba, 1-1-1 Tennodai, Tsukuba, Ibaraki 305-8577, Japan
[4]Department of Earth and Planetary Sciences, Faculty of Science, Kyushu University, Nishi-ku, Fukuoka 819-0395, Japan
*E-mail: s2630058@u.tsukuba.ac.jp

ORCID: 0009-0007-9629-4785, 0000-0002-0547-3208, 0000-0003-4271-4901

Abstract

To probe the role of hierarchical gas structures in massive star formation, we performed a statistical analysis of 13 Galactic star-forming regions using the FUGIN CO survey data. Applying a non-binary dendrogram algorithm to the position-position-velocity data, we extracted hierarchical structures and classified them into macroscopic trunks, internal leaves (the densest substructures nested within trunks), and isolated structures, comparing their properties with an analysis of variance controlling for regional differences. In representative regions, the trunks correspond to recognizable morphologies such as filaments and hub-filament systems, or to the kinematic signatures of structure-forming events such as cloud-cloud collisions that may produce them. Across the sample, the trunks are extended, massive, and strongly bound reservoirs, while the internal leaves are significantly more massive, denser, and more tightly bound than isolated structures of similar spatial scale. Comparing the structures with YSOs and Hi-GAL clumps, we find no statistically significant hierarchical dependence in the observed YSO population, whereas the leaves harbor significantly more clumps and a much larger total clump mass than isolated structures. Because the clump formation efficiency is comparable between the two, this enhancement follows from the larger gas reservoirs of the leaves rather than a higher local conversion rate. We interpret these contrasts, together with the inward gas motions in the position-velocity diagrams, in terms of a scenario in which the deep potential of the trunks sustains continuous accretion onto the leaves and promotes mutual interactions among them. These processes may raise the characteristic fragmentation mass, consistent with numerical predictions, channeling the gas into exceptionally massive clumps rather than a proportionally larger low-mass population. Our single-epoch data constrain only these structural contrasts, but indicate that the gas available for massive star formation is organized on scales larger than a single core.

Keywords: stars: formation — stars: massive — ISM: clouds — ISM: kinematics and dynamics — ISM: structure

1 Introduction

Massive stars ($> 8\ M_\odot$) play a crucial role in the evolution of the interstellar medium and host galaxies through intense stellar feedback, such as ultraviolet radiation and supernova explosions, as well as chemical enrichment. Despite their profound impact, the exact physical mechanisms and necessary conditions for massive star formation remain a fundamental unresolved issue in astrophysics. To address the theoretical difficulty of sustaining the required high mass accretion rates, various observational studies have investigated the dense structures within giant molecular clouds, which are the primary sites of massive star formation. Observationally, this dense gas is organized into filamentary structures that are ubiquitous in molecular clouds and serve as fundamental sites for star formation (e.g., Schneider & Elmegreen 1979; Goldsmith et al. 2008; André et al. 2010, see also André et al. 2014 for a review). Where multiple filaments converge, they form hub-filament systems (HFSs), whose central hubs have been widely recognized as exceptionally active environments for massive star and cluster formation (e.g., Myers 2009; Kumar et al. 2020). Such concentrations may in turn arise from dynamical processes that gather and compress the gas, and a variety of mechanisms have been proposed and observed to drive this convergence, including filament collisions (e.g., Nakamura et al. 2014; Kashiwagi et al. 2023, 2024), shock-driven compressions (e.g., Nozaki & Inutsuka 2026), and supersonic cloud-cloud collisions (CCCs) (e.g., Habe & Ohta 1992; Inoue & Fukui 2013; Inoue et al. 2018). In particular, CCCs have been frequently reported as a plausible trigger of massive star formation through rapid gas compression and massive clump formation, supported by extensive observational studies (e.g., Hasegawa et al. 1994; Furukawa et al. 2009; Fukui et al. 2014, 2016, see also Fukui et al. 2021 for a review). Therefore, characterizing both these dense structures and the dynamical processes that assemble them is essential for understanding the highly efficient mass accumulation processes required for massive star formation.

Molecular clouds, and the star-forming regions within them, exhibit a pronounced hierarchical structure over a wide range of spatial scales, in which smaller, denser structures are embedded within larger, more diffuse ones, extending from clouds and clumps down to the cores that form individual stars or small stellar groups (e.g., Houlahan & Scalo 1992). This hierarchical organization is naturally captured by multi-scale decompositions of the gas, such as dendrogram analyses, which have become a standard framework for characterizing molecular cloud structure (e.g., Rosolowsky et al. 2008; Goodman et al. 2009). How this nested structure relates to the assembly of stars, and of massive stars in particular, is nevertheless interpreted differently by competing the-

Received: , **Accepted:**

oretical frameworks, which make distinct predictions for the dynamical state and kinematics of the gas as a function of scale. In the turbulent core model, a massive star forms from a single, centrally condensed core that is supported against collapse by internal turbulence and remains in approximate virial equilibrium, so that the relevant structure is essentially set at the core scale (e.g., McKee & Tan 2002, 2003). In the competitive accretion picture, by contrast, stars form within a clump-scale gravitational potential and grow by accreting gas funneled toward the potential minimum, so that the clump, rather than an isolated core, sets the mass reservoir (e.g., Bonnell et al. 2001, 2004). In the global hierarchical collapse (GHC) scenario, molecular clouds undergo multi-scale gravitational contraction in which small-scale collapse proceeds within larger-scale collapse, channeling mass from cloud to clump to core across the nested hierarchy and implying that gravity becomes increasingly dominant over turbulent support toward smaller scales (e.g., Vázquez-Semadeni et al. 2009, 2019). A related conveyor-belt view further emphasizes that the gas feeding massive star formation may be continuously supplied by larger-scale inertial flows, rather than drawn from a fixed, locally bound reservoir (e.g., Padoan et al. 2020). Because these frameworks are not mutually exclusive but differ mainly in whether the gas is gravitationally bound at each scale and in whether continuous flows link successive scales, measuring how the virial state and internal kinematics of the structures change from large to small scales—across a large sample—provides a useful observational means of constraining their relative roles, rather than of singling out any single scenario (e.g., Ballesteros-Paredes et al. 2011).

Motivated by these scale-dependent predictions, recent observational studies have increasingly applied dendrogram decompositions to characterize the hierarchical properties of molecular clouds across multiple scales and to assess the role of self-gravity within them. For instance, Shen et al. (2024) and He et al. (2026) analyzed the quiescent Maddalena's Cloud and the active Rosette Molecular Cloud, respectively. These works, however, have characterized the hierarchy largely in a mathematical sense. The Rosette Molecular Cloud, for example, is known to host a hub-filament system and kinematic signatures attributed to a cloud-cloud collision (e.g., Schneider et al. 2012; Li et al. 2018), yet its dendrogram analysis did not examine how the extracted hierarchy relates to these recognizable morphological structures and dynamical signatures, leaving the physical meaning of these mathematically defined structures unclear. At the same time, because these analyses remain confined to individual clouds and focus on their general scaling relations, the systematic behavior of the hierarchical structure across the diverse population of Galactic molecular clouds is still largely unexplored. Addressing the former calls for examining, in selected regions amenable to a qualitative physical characterization, how the extracted hierarchy is realized in the actual structure of a cloud, thereby grounding the mathematically defined decomposition in recognizable physical phenomena. Addressing the latter requires moving beyond individual case studies toward a uniform analysis of a large and varied sample of Galactic molecular clouds, from which the systematic and intrinsic properties of the hierarchical structure can be established and compared with the theoretical frameworks introduced above.

To address these requirements, this study bridges the mathematically extracted hierarchical structures and their physical meaning by combining a qualitative characterization of selected regions with a statistical treatment across a large sample. Using the FUGIN CO survey data (Umemoto et al. 2017), we target 13 Galactic star-forming regions in which a variety of active dynamical gas motions have been observationally suggested. Applying a dendrogram algorithm to the three-dimensional CO line data, we extract the hierarchical structures across this sample in a uniform manner. For selected regions amenable to a qualitative characterization, we map the extracted hierarchies onto the physical gas distribution to examine how they correspond to recognizable morphological structures and kinematic signatures. Across the full sample, we then statistically characterize how the intrinsic physical properties of the hierarchies behave as a function of scale, and compare these systematic trends with the theoretical frameworks introduced above in order to place observational constraints on them. Finally, by cross-matching these hierarchical structures with point-source catalogs of young stellar objects and dense clumps, we assess how the macroscopic hierarchical structure relates to the sites of star formation, with particular attention to the early stages of massive star formation.

The remainder of this paper is organized as follows. Section 2 describes the observational data utilized in this study, including the FUGIN CO survey, the SPICY YSO catalog, and the Hi-GAL clump catalog. In Section 3, we detail the methodology for extracting the hierarchical structures using the dendrogram algorithm, evaluating their physical properties, and assessing their spatial associations with point sources. Section 4 presents the results of our statistical analyses, including the morphological and kinematic characteristics, comparisons of physical properties among structural categories, and star formation activities. In Section 5, based on these findings, we discuss the physical mechanisms of hierarchical mass accumulation and how massive star formation varies across the diverse dynamical environments in our sample. Finally, Section 6 summarizes the main conclusions of this study.

2 Data

2.1 FUGIN

In this study, we used the ^{12}CO ($J = 1 - 0$), ^{13}CO ($J = 1 - 0$), and C^{18}O ($J = 1 - 0$) emission line data obtained from the FUGIN (FOREST Unbiased Galactic plane Imaging survey with the Nobeyama 45-m telescope) project (Umemoto et al. 2017). The observations were conducted using the Nobeyama Radio Observatory (NRO) 45 m telescope, equipped with the four-beam, dual-polarization, sideband-separating receiver FOREST (Minamidani et al. 2016). The SAM45 digital spectrometer (Kuno et al. 2011; Kamazaki et al. 2012) was employed as the back-end, providing a frequency resolution of 244.14 kHz, which corresponds to a velocity resolution of 0.65 km s^{-1} at 115 GHz. The effective velocity resolution of the data is 1.3 km s^{-1}. The half-power beam width (HPBW) of the NRO 45 m telescope is 14″ at 115 GHz for ^{12}CO ($J = 1 - 0$) and 15″ at 110 GHz for ^{13}CO ($J = 1 - 0$) and C^{18}O ($J = 1 - 0$). After convolving the data with a Bessel-Gaussian function during the gridding process, the effective angular resolution of the final data cubes is approximately 20″. The typical system noise temperatures ($T_{\rm sys}$) during the observations were ∼250 K for ^{12}CO ($J = 1 - 0$) and ∼150 K for ^{13}CO ($J = 1 - 0$) and C^{18}O ($J = 1 - 0$). The antenna temperature scale was calibrated using the standard chopper-wheel method, and then converted to the main-beam temperature ($T_{\rm mb}$) scale using main beam efficiencies ($\eta_{\rm mb}$) of 0.43 for ^{12}CO ($J = 1 - 0$), and 0.45 for ^{13}CO ($J = 1 - 0$) and C^{18}O ($J = 1 - 0$).

We extracted 13 sub-regions from the full survey data, targeting active star-forming regions. To ensure a consistent spatial scale for the structural analysis across regions located at different distances,

Table 1. Summary of the targeted regions and typical noise levels.

Region Name	l range [degree]	b range [degree]	$V_{\rm LSR}$ [km s^{-1}]	Distance [kpc]	Resolution [arcsec]	$T_{\rm rms}$ [K] ^{12}CO	^{13}CO	C^{18}O
G18	$[17.80, 18.80]$	$[-0.80, 0.00]$	$[25, 75]$	$6.07 \pm 0.13^{(1)}$	37	2.27	0.51	0.34
G45	$[45.00, 45.60]$	$[-0.20, 0.30]$	$[50, 70]$	$8^{(2)}$	28	1.55	0.44	0.30
M16	$[16.60, 17.40]$	$[0.10, 0.99]$	$[14, 30]$	$1.8^{(3)}$	123	2.35	0.30	0.10
M17	$[14.70, 15.50]$	$[-0.80, -0.30]$	$[0, 30]$	$2.04^{+0.16}_{-0.17}{}^{(4)}$	109	1.38	0.22	0.10
N4	$[11.74, 12.00]$	$[0.65, 0.99]$	$[20, 30]$	$2.80 \pm 0.30^{(5)}$	79	4.74	1.01	0.23
N14	$[13.70, 14.90]$	$[-0.60, 0.10]$	$[30, 50]$	$3.1^{(6)}$	72	2.83	0.61	0.23
N35	$[24.10, 24.70]$	$[-0.10, 0.50]$	$[100, 130]$	$8.8 \pm 0.3^{(7)}$	25	3.46	1.08	0.73
Sh2-48	$[16.30, 16.90]$	$[-0.60, -0.10]$	$[30, 60]$	$3.8 \pm 0.2^{(8)}$	58	2.09	0.72	0.17
W33	$[12.50, 13.50]$	$[-0.50, 0.50]$	$[30, 45]$	$2.40^{+0.17}_{-0.15}{}^{(9)}$	93	3.87	0.66	0.13
W39	$[18.70, 19.00]$	$[-0.60, -0.30]$	$[40, 75]$	$4.5 \pm 0.2^{(10)}$	49	2.59	0.56	0.30
W43	$[30.20, 31.20]$	$[-0.50, 0.50]$	$[70, 120]$	$5.49^{+0.39}_{-0.34}{}^{(11)}$	40	3.81	0.67	0.33
W49 N	$[42.80, 43.40]$	$[-0.40, 0.20]$	$[-5, 20]$	$11.11^{+0.79}_{-0.69}{}^{(12)}$	20	1.49	0.53	0.48
W51 A	$[48.70, 49.70]$	$[-0.70, 0.30]$	$[40, 75]$	$5.41^{+0.31}_{-0.28}{}^{(13)}$	41	1.34	0.33	0.23

Notes. Columns are as follows: (1) Region name. (2)-(3) Galactic longitude and latitude ranges of the extracted data cubes. (4) Velocity range of the integrated data cube. (5) Distance to the region. (6) Effective angular resolution after the smoothing process. (7)-(9) Typical root-mean-square noise levels for ^{12}CO ($J = 1 - 0$), ^{13}CO ($J = 1 - 0$), and C^{18}O ($J = 1 - 0$) data cubes, respectively, evaluated at a velocity resolution of 0.65 km s^{-1}.
References. (1) Sofue (2023); (2) Urquhart et al. (2018); Bhadari et al. (2022); (3) Bonatto et al. (2006); Dufton et al. (2006); Guarcello et al. (2007); (4) Chibueze et al. (2016); (5) Fujita et al. (2019); (6) Urquhart et al. (2018) (7) Anderson & Bania (2009); Torii et al. (2018); (8) Ortega et al. (2013); Torii et al. (2021); (9) Immer et al. (2013); (10) Kerton et al. (2013); (11) Zhang et al. (2014); (12) Zhang et al. (2013); (13) Sato et al. (2010).

we applied a two-dimensional Gaussian smoothing to the data cubes. This smoothing process was performed using the `imsmooth` task in the Common Astronomy Software Applications (CASA) package (CASA Team et al. 2022). Specifically, we matched the physical resolution of all regions to that of the most distant target, W49 N (11.11 kpc), which corresponds to a uniform physical resolution of ~ 1.08 pc. Thus, the target angular resolution for a region at a distance of d kpc was set to $20'' \times (11.11/d)$, where $20''$ is the original effective angular resolution of the FUGIN data. The boundaries of the extracted areas, adopted distances, and the effective angular resolutions after smoothing for each region are summarized in Table 1. Because the spatial smoothing alters the noise characteristics, we independently estimated the $T_{\rm rms}$ for each targeted region after the smoothing process. These evaluated $T_{\rm rms}$ values are also listed in Table 1.

2.2 SPICY YSO catalog

To evaluate the star formation activity within our targeted molecular clouds, we utilized the Spitzer/IRAC Candidate YSO (SPICY) catalog (Kuhn et al. 2021). This catalog provides a comprehensive list of young stellar object (YSO) candidates across the Galactic midplane, identified based on mid-infrared photometry from the Spitzer Space Telescope. From the full catalog, we extracted the sources located within the specific Galactic longitude and latitude ranges defined for each of our 13 targeted regions.

To ensure the reliability of the sample and focus on the active early stages of star formation, we applied a strict classification filter, retaining only the sources categorized as Class I and Class II YSOs. It should be noted that while such clear evolutionary classifications are well-established for low-mass young stellar objects, applying a similarly straightforward scheme to high-mass stars is highly challenging due to their rapid evolution while deeply embedded in their natal clouds (Motte et al. 2018). Consequently, the use of this filtered catalog explicitly restricts our analysis to tracing the early stages of low-mass star formation within our targeted molecular clouds.

2.3 Hi-GAL clump catalog

To evaluate the early stages of high-mass star formation within our targeted molecular clouds, we utilized the physical property catalog of dense clumps identified by the *Herschel* Infrared Galactic Plane Survey (Hi-GAL) (e.g., Elia et al. 2017, 2021). As highlighted by Molinari et al. (2016) and Motte et al. (2018), Hi-GAL serves as a reference survey for tracing the earliest phases of high-mass star-forming sites across the Galactic plane. The five far-infrared and submillimeter bands of *Herschel* provide the capability to trace both the column density and temperature of dusty cloud fragments that act as precursors to massive stars and stellar clusters. While the SPICY catalog traces individual low-mass young stellar objects, the spatial resolution of Hi-GAL is primarily suited to resolving clumps with typical sizes of $\sim$0.5 pc, which correspond to the scale of protoclusters rather than individual stellar cores (Beltrán et al. 2013; Motte et al. 2018).

Similar to the procedure applied to the SPICY catalog, we first extracted the clumps located within the specific Galactic longitude and latitude ranges defined for each of our 13 targeted regions. To minimize contamination from foreground and background sources along the line of sight, we implemented an additional distance-based filtering process. For clumps with kinematically derived distances in the catalog, we retained only those consistent with the adopted distance of each targeted region, allowing for a typical uncertainty margin (e.g., 20% or a minimum of 0.5 kpc). Clumps without available distance estimates in the catalog were conservatively retained under the assumption that they are physically associated with the prominent targeted molecular clouds. By utilizing this curated clump catalog, we aim to trace the initial conditions and large-scale precursors of high-mass star formation, providing a clear contrast to the low-mass star formation activity traced by the YSO sample.

Table 2. Dendrogram parameters.

Region	min_value [σ]	min_npix [voxels]
G18	9.4	98
G45	5.6	50
M16	17.2	1058
M17	13.1	800
N4	4.3	392
N14	7.2	338
N35	6.8	50
Sh2-48	6.4	242
W33	7.6	578
W39	10.3	162
W43	7.2	128
W49 N	3.9	32
W51 A	8.5	128

Notes. Columns are as follows: (1) Region name. (2) The lowest intensity threshold, determined by the 99.9th percentile of the boundary pixels, expressed as a multiple of the local root-mean-square noise (σ). (3) The minimum number of voxels required for an independent structure, calculated as $(1.5\theta/8.5'')^2 \times 2$.

3 Method

3.1 Dendrogram

To practically implement the dendrogram analysis and extract the hierarchical structures from our data, we utilized the Python package `astrodendro` (Rosolowsky et al. 2008), which is part of the `Astropy` ecosystem (Astropy Collaboration et al. 2013, 2018, 2022). This tool systematically decomposes the 3D position-position-velocity (PPV) data cubes into interconnected hierarchies based on three user-defined parameters: `min_value`, `min_delta`, and `min_npix`.

The algorithm begins by locating local emission maxima within the dataset. It then progressively lowers the intensity threshold, defining 3D isosurfaces that enclose these maxima. When two adjacent isosurfaces merge at a specific intensity level, the algorithm checks whether the enclosed structures satisfy the independence criteria. A structure is considered independent if the difference between its local maximum intensity and the merging level is greater than `min_delta`, and if the number of voxels contained within the structure exceeds `min_npix`.

Based on this hierarchical tree, the identified independent structures are initially classified into four categories: leaves, branches, trunks, and isolated structures. Structures that reside at the top of the hierarchy and contain no further internal substructures are defined as "leaves", representing the densest local gas concentrations. When leaves or other intermediate structures merge at lower intensity levels, they form larger parent structures called "branches". The largest continuous structures located at the very base of the hierarchy, originating directly from the `min_value` threshold, are defined as "trunks". Trunks typically encompass multiple internal branches and leaves, tracing the extended, large-scale parental gas. Furthermore, structures that satisfy the independence criteria but exhibit no internal hierarchical sub-divisions (i.e., they act as both the base and the top of their own hierarchy) are classified as "isolated" structures.

To mitigate artificial fragmentation caused by noise fluctuations, we applied a custom pruning process to the initial dendrogram tree. While the concept of a non-binary dendrogram algorithm was originally introduced by Storm et al. (2014) with a different technical implementation, our custom approach is inspired by recent works (Shen et al. 2024; He et al. 2026). Specifically, as schematically illustrated in Figure 1, we dissolved intermediate structures (branches and trunks) whose intensity span (ΔI, the difference between their upper formation level and lower merging level) was below a user-defined threshold, `prune_delta`. The independent children of these dissolved structures were then directly re-assigned to their nearest valid ancestral parent. This restructuring process bypasses insignificant intermediate boundaries, effectively allowing non-binary mergers. Although branches are naturally identified and reorganized during this tree construction, our subsequent analysis primarily focuses on leaves, trunks, and isolated structures to characterize the distinct physical states at the extremes of the hierarchy.

Because our targeted regions were extracted from the larger Galactic plane survey, physical gas emissions naturally extend beyond the boundaries of the 3D data cubes. To handle these truncated structures and ensure the high reliability of the derived physical properties, we implemented an adaptive thresholding and filtering approach. First, to proactively prevent structures from being artificially truncated at the edges, we adaptively set the lowest intensity threshold, `min_value`, for each region. Specifically, we extracted all pixels along the six boundary faces (both spatial and spectral) and adopted their 99.9th percentile intensity value as the `min_value`. Instead of using the absolute maximum, adopting the 99.9th percentile effectively ignores anomalous noise spikes that would otherwise excessively raise the threshold and obscure meaningful internal gas signals. By establishing this robust upper limit for the boundary emission, most hierarchical structures naturally close within the data cube before colliding with the edges. Second, as a strict filtering measure, any structures that still touched the boundaries by even a single voxel, along with all their internal descendants, were entirely excluded from our final catalog. For the remaining structures, the structural independence was evaluated based on the local noise level (1σ). We set the minimum peak-to-merging intensity difference, `min_delta`, and the pruning threshold, `prune_delta`, both to 1σ.

Finally, the minimum number of voxels, `min_npix`, was defined to ensure that the identified structures are sufficiently resolved both spatially and spectrally. Following the criterion proposed by Shen et al. (2024), we required the robust structures to have a spatial extent of at least 1.5 times the effective angular resolution (θ) and a spectral extent spanning at least 2 velocity channels. Given the spatial pixel size of $8.5''$ in the FUGIN data, this threshold is calculated as $\texttt{min\_npix} = (1.5\theta/8.5'')^2 \times 2$. Since θ varies among the targeted regions due to the spatial smoothing process (see Table 1), the adopted `min_npix` values were calculated and adjusted region by region. The specific values of `min_value` and `min_npix` for each region are summarized in Table 2.

3.2 Physical properties of the identified structures

To characterize the identified hierarchical structures, we derived their fundamental physical properties: effective radius, mass, volume density, and virial parameter.

First, the effective radius, R, of each structure was estimated from its spatial footprint. We projected the three-dimensional mask of each identified structure onto the two-dimensional position-position plane. The effective radius was then calculated as

$$R = \sqrt{\frac{A}{\pi}} \quad [\mathrm{pc}], \tag{1}$$

where A is the exact physical area of the projected two-

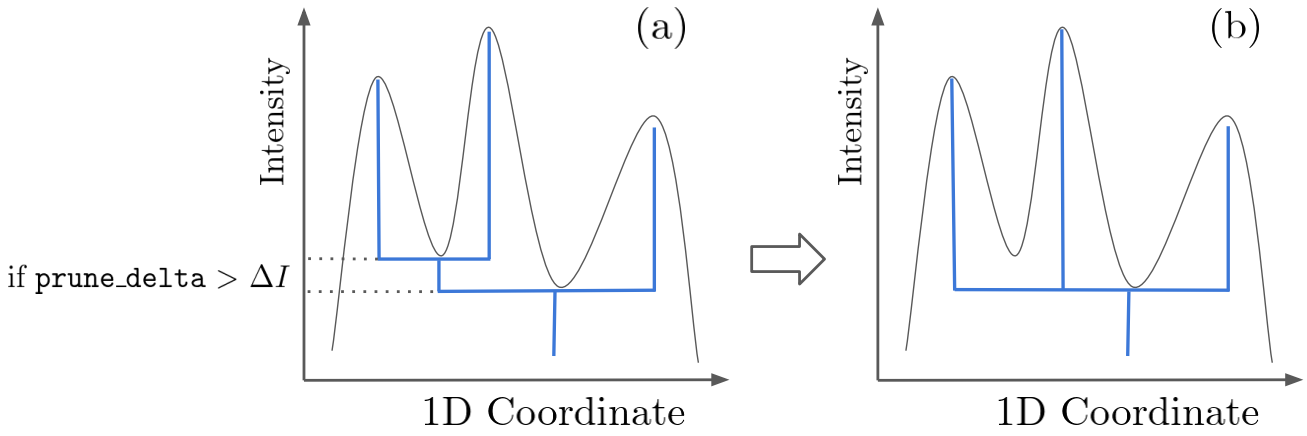

Fig. 1. Schematic diagram illustrating the custom pruning process applied to the dendrogram tree. The grey solid curve represents a hypothetical one-dimensional intensity profile of the gas emission. The blue lines indicate the corresponding hierarchical tree structures identified by the dendrogram algorithm. (a) The initial tree structure. If an intermediate structure (branch) has an intensity span (ΔI, defined as the difference between its upper formation level and lower merging level) smaller than the user-defined threshold, `prune_delta`, it is flagged for removal. (b) The resulting tree after the pruning process. The flagged intermediate structure (branch) is dissolved, and its independent children (leaf) are directly re-assigned to the nearest valid ancestral parent (trunk), effectively resulting in a non-binary merger. Alt text: Two-panel schematic labeled a and b, each plotting intensity against a one-dimensional coordinate with a two-peaked curve and an overlaid tree of nested structures. Between panels a and b, one short intermediate branch is removed and its substructure connects directly to the base.

dimensional mask.

Second, we calculated the local thermodynamic equilibrium (LTE) mass, M, for each structure using the ^{12}CO ($J=1-0$) and ^{13}CO ($J=1-0$) emission lines. Assuming the ^{12}CO ($J=1-0$) emission is optically thick, we derived the excitation temperature from the peak main-beam temperature of the ^{12}CO ($J=1-0$) line. Under the assumption of LTE, we calculated the optical depth of the ^{13}CO ($J=1-0$) line and subsequently determined the ^{13}CO ($J=1-0$) column density. The H_2 column density, $N(H_2)$, was estimated by adopting a typical abundance ratio of $[H_2]/[^{13}CO] = 5\times10^5$ (Dickman 1978). The total mass of the structure is given by

$$M = \mu m_{\rm H} A_{\rm pix} \sum N(H_2) \quad [M_\odot], \tag{2}$$

where $\mu = 2.8$ is the mean molecular weight per hydrogen molecule, $m_{\rm H}$ is the mass of a hydrogen atom, and $A_{\rm pix}$ is the physical area of a single pixel. The summation is performed over all valid pixels within the projected mask.

Third, assuming a simple spherical geometry, the volume density, ρ, of each structure was calculated as

$$\rho = \frac{M}{\frac{4}{3}\pi R^3} \quad [\mathrm{g\ cm^{-3}}]. \tag{3}$$

Finally, to evaluate the dynamical state and gravitational stability of the structures, we derived the virial parameter, $\alpha_{\rm vir}$ (Bertoldi & McKee 1992). The virial parameter is defined as

$$\alpha_{\rm vir} = \frac{5\sigma_v^2 R}{GM}, \tag{4}$$

where G is the gravitational constant. The one-dimensional velocity dispersion, σ_v, was determined by extracting the average spectrum of the structure using its three-dimensional mask and fitting a single Gaussian profile to the spectrum.

3.3 Association with point sources

To investigate the star formation activity within the identified hierarchical structures, we evaluated their spatial association with the YSOs and dense clumps extracted from the catalogs described in Section 2. Since these catalogs provide two-dimensional spatial coordinates (Galactic longitude and latitude), we projected the three-dimensional mask of each identified dendrogram structure onto the two-dimensional position-position plane. A point source was considered to be physically associated with a structure if its coordinates fell within the projected two-dimensional boundary of the structure.

For the YSO sample, which traces low-mass star formation, we applied a statistical background subtraction method to account for field contamination. First, we defined the "ON" region as the total projected area covered by all the identified trunks within a given targeted cloud. Consequently, the remaining area within the field of view was defined as the "OFF" region, representing the ambient background. We calculated the local background YSO surface density by dividing the number of YSOs located in the OFF region by its physical area. For each individual structure, the expected number of background YSOs was estimated by multiplying this background density by the projected physical area of the structure. Finally, the true number of associated YSOs for each structure was derived by subtracting the expected background number from the raw count of YSOs found within its boundary.

In contrast, for the Hi-GAL clump catalog, which traces the precursors of high-mass star formation, we adopted a direct spatial matching approach. Since the Hi-GAL clumps specifically identify dense gas condensations deeply embedded within molecular clouds, the contamination from ambient background sources is considered negligible compared to the relatively widespread YSO distribution. Therefore, the number of associated clumps was directly determined by counting the sources located within the pro-

jected mask of each structure without applying the background subtraction process. Although Hi-GAL clumps inherently possess finite physical sizes, we treated them as point sources located at their cataloged central coordinates for the spatial matching process. Therefore, both the number and total mass of clumps associated with a structure are derived strictly from the clumps whose centers fall within the projected boundary, without accounting for partial spatial overlaps at the edges.

To quantitatively evaluate the efficiency of mass conversion into stellar and pre-stellar objects, we define the Star Formation Efficiency (SFE) and Clump Formation Efficiency (CFE) for each identified structure. For low-mass star formation, because the mass of the identified YSOs is no longer in the molecular gas phase, this mass is entirely absent from the total gas mass ($M_{\rm gas}$) traced by our CO observations. Therefore, following standard approaches (Evans et al. 2009), we calculate the SFE by comparing the total stellar mass to the initial total mass (stellar plus gas). Assuming a typical average mass of $0.5\ M_\odot$ for each YSO (Evans et al. 2009), the SFE is defined as:

$$\mathrm{SFE} = \frac{M_{\rm YSO}}{M_{\rm YSO} + M_{\rm gas}} = \frac{0.5\ M_\odot \times N_{\rm YSO}}{0.5\ M_\odot \times N_{\rm YSO} + M_{\rm gas}}, \quad (5)$$

where $N_{\rm YSO}$ is the background-subtracted number of associated YSOs, and M_{gas} is the LTE gas mass of the structure derived in Section 3.2.

In contrast, the dense clumps identified by Hi-GAL are primarily composed of gas and dust that are still deeply embedded within the parental cloud. Because the mass of these clumps is inherently included within the total gas mass ($M_{\rm gas}$) traced by our CO observations, we define the CFE simply as the mass fraction of the dense clumps relative to the total structure mass:

$$\mathrm{CFE} = \frac{M_{\rm clump}}{M_{\rm gas}}, \quad (6)$$

where $M_{\rm clump}$ is the total mass of the associated Hi-GAL clumps. These clump masses are taken from the Hi-GAL physical catalog, where they were derived through spectral energy distribution (SED) fitting of the dust continuum emission (Elia et al. 2017, 2021).

4 Result

4.1 Morphology and kinematics of representative regions

In this subsection, we examine, for several selected regions in which the hierarchical structures can be interpreted qualitatively, how the dendrogram-identified structures are realized in the actual gas distribution and kinematics. To this end, we present position–position (PP) and position–velocity (PV) diagrams, defined as velocity-integrated and spatially integrated intensity maps, respectively, and overlay on them the contours of the identified structures. This allows us to illustrate how the mathematically defined hierarchical decomposition corresponds both to recognizable morphological structures together with the internal inflow kinematics they organize—such as filaments and hub-filament systems within which gas contraction and infall proceed—and to the kinematic signatures of structure-forming events that do not presuppose any particular morphology, such as cloud–cloud collisions, thereby grounding it in physical terms before the statistical analysis of the full sample.

4.1.1 Correspondence with morphologies and internal inflow

In the following two regions, the identified hierarchy corresponds to a recognizable morphological structure together with the internal inflow it hosts: the trunk traces the overall morphology, the leaves pick out the dense gas concentrations within it, and the velocity field reveals gas streaming inward through that morphology.

Figures 2(a) and (b) present the PP and PV diagrams of the N14 region, respectively, overlaid with the contours of our identified structures. This region displays an extended, filamentary morphology, which the encompassing trunk structure traces as the broad parental gas. Dewangan et al. (2020) revealed characteristic oscillatory velocity structures in the PV diagram of this region, interpreting this kinematical feature as evidence of ongoing hierarchical gas contraction within the filamentary structure. As shown in Figure 2(b), the hierarchies identified by our dendrogram analysis successfully trace these oscillatory velocity patterns. Figure 3 further illustrates this correspondence by overlaying the expected oscillatory patterns (cyan dashed curves) onto our identified structures. Specifically, the leaf structures correspond well to the individual dense gas clumps at the peaks of the velocity oscillations, while the encompassing trunk traces the broader gas exhibiting the global oscillating motion. In this region, the dendrogram hierarchy thus maps onto the filamentary morphology and the multi-scale contraction within it that Dewangan et al. (2020) interpreted as hierarchical gas contraction.

Figures 4(a) and (b) present the PP and PV diagrams of the W33 region, respectively, overlaid with the contours of our identified structures. Liu et al. (2021) identified an HFS in this region, characterizing its morphology as a central hub with radial filaments. As shown in the PP diagram (Figure 4(a)), our dendrogram-identified hierarchies agree well with this reported structure. Specifically, the leaf structures trace the dense gas concentrations both within the central hub and along the filaments, appearing as clumpy substructures that are visually consistent with filament fragmentation. The encompassing trunk structure outlines the overall system, tracing the radial filaments extending from the central hub. The PV diagram (Figure 4(b)) further shows velocity gradients along these filaments, consistent with gas inflow toward the central hub. Our identified structures capture this kinematic pattern, tracing a spatially and kinematically continuous structure from the outer filaments to the central hub.

In both regions, therefore, the dendrogram hierarchy maps onto a recognizable morphology—a contracting filament in N14 and a hub-filament system in W33—together with the internal inflow that morphology organizes, thereby grounding the decomposition in physical terms.

4.1.2 Correspondence with cloud–cloud collisions

In the following two regions, by contrast, the identified hierarchy corresponds not to a fixed morphology but to the kinematic signature of a cloud–cloud collision—a structure-forming event that does not presuppose any particular morphology: the trunks enclose the interacting velocity components as continuous hierarchies, while the leaves pick out the dense gas concentrations associated with the collision.

Figures 5(a) and (b) present the PP and PV diagrams of the W51 A region, respectively, overlaid with the contours of our identified structures. The PV diagram (Figure 5(b)) reveals multiple velocity components connected by a broad velocity bridge. Fujita et al. (2021) suggested a CCC in this region, as such bridge features are considered typical kinematic signatures of these interactions. In this kinematically complex region, the leaf structures identified by our dendrogram analysis are distributed across these distinct velocity components. The encompassing trunk structure spans these multiple components and the connecting bridge, enclosing

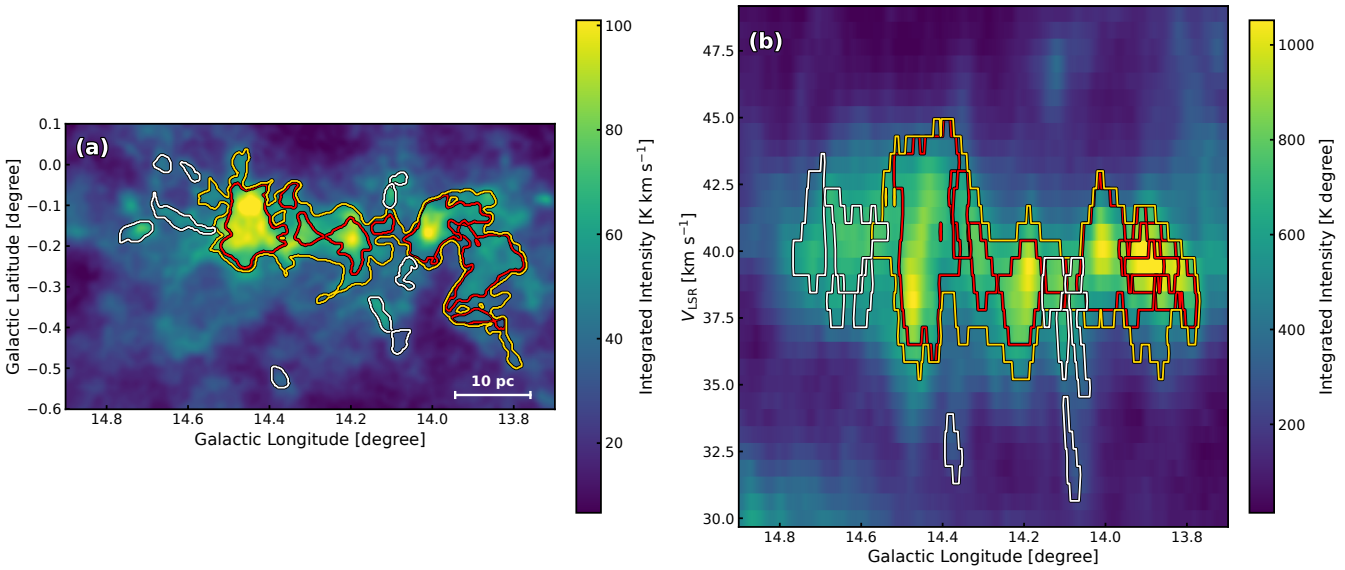

Fig. 2. (a) Position-position (PP) diagram and (b) position-velocity (PV) diagram of the N14 region. The background color map represents the integrated intensity of the gas emission. The contours indicate the projected hierarchical structures identified by the dendrogram analysis: leaf (red), trunk (yellow), and isolated (white) structures. Alt text: Two-panel view of the N14 region, with panel a a position-position map and panel b a position-velocity map, each showing background emission intensity overlaid with contours of leaf, trunk, and isolated structures. The leaf contours enclose the brightest compact peaks nested inside a larger trunk contour that follows the extended elongated emission, while the isolated contours lie separately over fainter clumps.

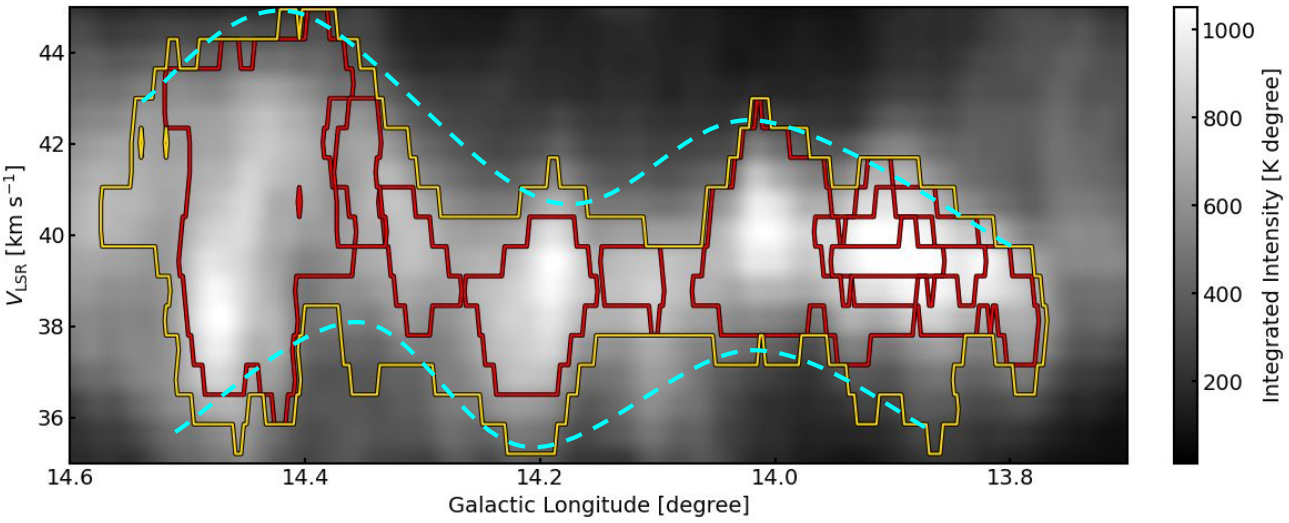

Fig. 3. Position-velocity (PV) diagram of the N14 region. The background color map is identical to Figure 2(b), and the overlaid contours show only the leaf and trunk structures, while the isolated structures are omitted for clarity. The cyan dashed curves are arbitrarily drawn to indicate the expected oscillatory gas motions. Alt text: Single-panel position-velocity map of the N14 region, plotting velocity against Galactic longitude, with background emission intensity and overlaid contours of leaf and trunk structures. Wavy dashed curves run across the map, arbitrarily tracing a repeating up-and-down oscillation that follows the velocity pattern outlined by the contours.

the scattered leaves within a single continuous hierarchy.

Figures 6(a) and (b) present the PP and PV diagrams of the N35 region, respectively, overlaid with the contours of our identified structures. Torii et al. (2018) reported an interaction between high-velocity and low-velocity gas components in this region, characterized by a steep velocity gradient in the PV diagram. As seen in Figure 6(b), the hierarchies identified by our dendrogram analysis are distributed along this steep velocity gradient. Specifically, two distinct trunk structures emerge along the gradient—one at higher Galactic longitudes and velocities, the other at lower values—whose internal leaf structures highlight the densest gas concentrations associated with this interaction.

In both regions, therefore, the dendrogram hierarchy encloses within continuous hierarchies the gas attributed to cloud–cloud collisions—the bridged velocity components in W51 A and the steep velocity gradient in N35—thereby grounding the decompo-

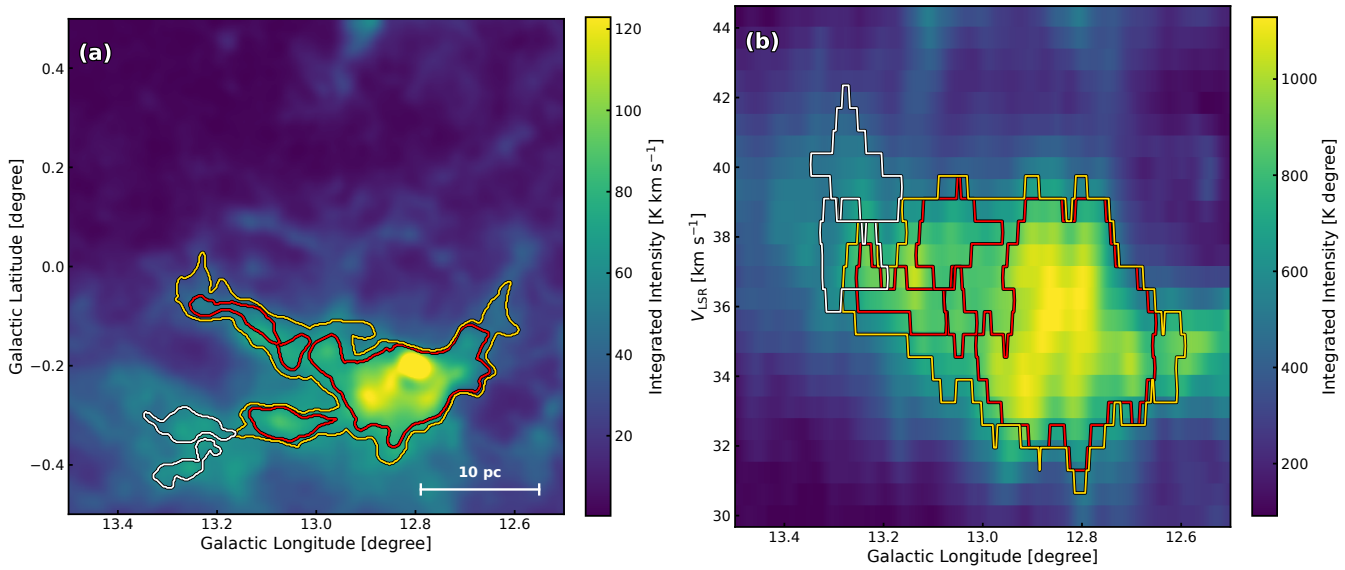

Fig. 4. Same as Figure 2, but for the W33 region. Alt text: Two-panel view of the W33 region, with panel a a position-position map and panel b a position-velocity map, each showing background emission intensity overlaid with contours of leaf, trunk, and isolated structures. The leaf contours mark dense knots in a central concentration and along filaments radiating from it, all enclosed within a single trunk contour outlining the whole filamentary system, while the isolated contours lie separately outside.

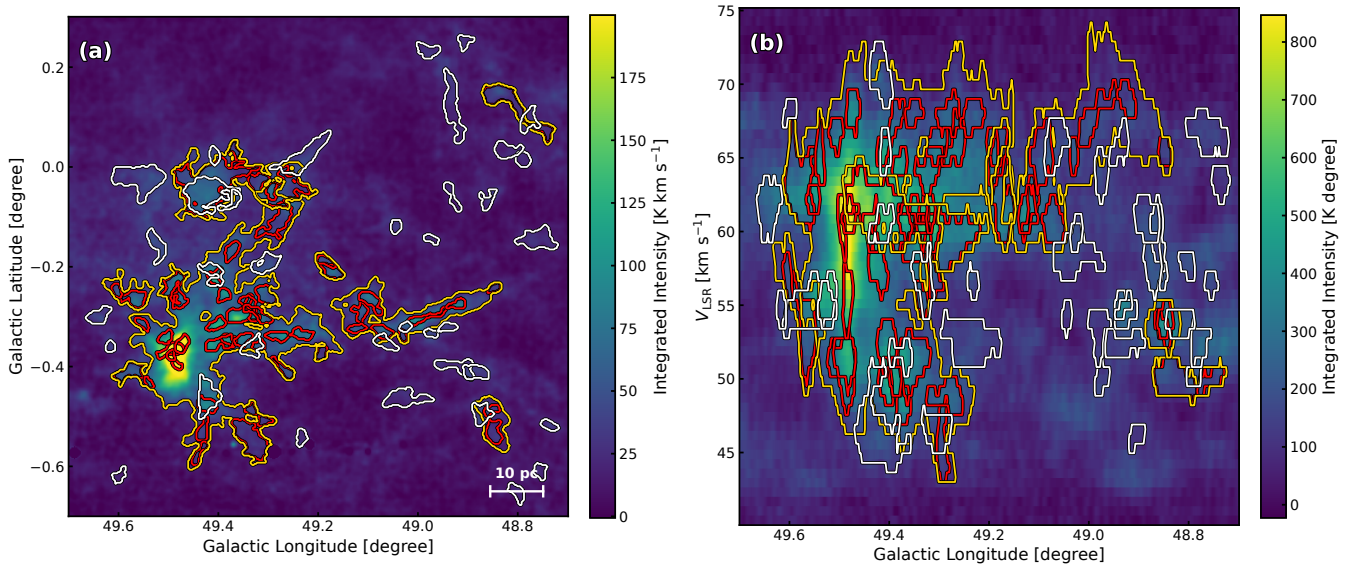

Fig. 5. Same as Figure 2, but for the W51 A region. Alt text: Two-panel view of the W51 A region, with panel a a position-position map and panel b a position-velocity map, each showing background emission intensity overlaid with contours of leaf, trunk, and isolated structures. The leaf contours are scattered over several distinct clumps that, in the position-velocity panel, separate into multiple velocity components joined by a broad connecting bridge; a single trunk contour spans all of these, while the isolated contours lie separately outside.

sition in physical terms.

4.2 Physical properties of the identified structures

Figure 7 displays the probability histograms of the physical properties (effective radius, mass, volume density, and virial parameter) for the three identified structural categories: trunks, leaves, and isolated structures. As seen in the histograms, trunks generally exhibit larger effective radii and masses compared to the other structures. Regarding volume density, a subtle increasing trend from trunks to isolated structures, and ultimately to leaves, is weakly apparent. However, because the fundamental physical conditions vary significantly across the target regions, the overall distributions of these properties exhibit substantial overlap. This region-to-region variance obscures the intrinsic differences between the structural categories, making visual distinction challenging.

To accurately compare the intrinsic physical properties across the structural categories, we must account for the significant environmental variance originating from the different host regions. We model the base-10 logarithmic value of a given physical property,

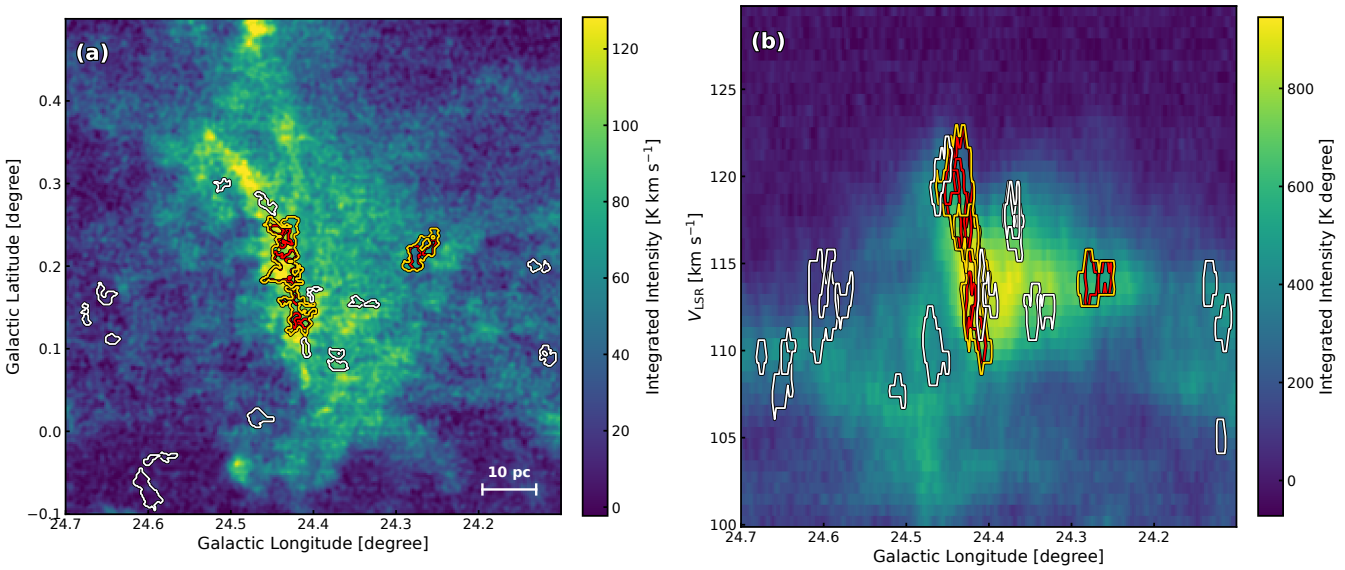

Fig. 6. Same as Figure 2, but for the N35 region. Alt text: Two-panel view of the N35 region, with panel a a position-position map and panel b a position-velocity map, each showing background emission intensity overlaid with contours of leaf, trunk, and isolated structures. In the position-velocity panel the emission follows a steep velocity gradient, along which two separate trunk contours are arranged, one at higher longitude and velocity and the other at lower values; each encloses its own leaf contours, while the isolated contours lie separately outside.

y, as a linear combination of the global mean (μ), the environmental baseline of the host region ($\alpha_{\rm region}$), the intrinsic effect of the structural category ($\beta_{\rm structure}$), and a residual error (ϵ):

$$y = \mu + \alpha_{\rm region} + \beta_{\rm structure} + \epsilon. \quad (7)$$

The parameters of this linear model were estimated using the ordinary least squares (OLS) method. To isolate and compare the pure structural differences, we calculated an adjusted logarithmic value, $y_{\rm adj}$, for each structure by subtracting the estimated regional baseline effect from the raw value:

$$y_{\rm adj} = y - \alpha_{\rm region} = \mu + \beta_{\rm structure} + \epsilon. \quad (8)$$

Using these adjusted values effectively removes the inherent baseline offsets of the different regions, enabling a direct and robust comparison of the structural categories. Finally, to quantitatively assess the statistical significance of the observed structural effect ($\beta_{\rm structure}$), we performed a Type II analysis of variance (ANOVA) on this linear model, which strictly evaluates the structural variance while controlling for regional dependence. A detailed description of this statistical modeling, including the parameter estimation via OLS and the formal derivation of the adjusted values, is provided in the Appendix.

4.2.1 Trunks vs. isolated structures

To investigate the macroscopic characteristics of clouds harboring internal hierarchies, we compare trunks and isolated structures based on their adjusted physical properties ($y_{\rm adj}$). Figure 8 presents these adjusted distributions and the corresponding ANOVA results, highlighting the statistical differences between the two structural categories.

As shown in Figures 8(a) and (b), trunks exhibit significantly larger adjusted effective radii and masses compared to isolated structures. Furthermore, the ANOVA reveals that trunks have significantly lower adjusted virial parameters than isolated structures (Figure 8(d)). These quantitative results demonstrate that trunks represent more extended, massive, and tightly gravitationally bound macroscopic systems. This strongly suggests that such large-scale, massive environments are physically required to harbor internal hierarchical structures.

In contrast, the adjusted volume density of trunks is significantly lower than that of isolated structures (Figure 8(c)). This difference inherently arises from their structural definitions: while isolated structures predominantly trace independent high-density regions without extended envelopes, trunks encompass both internal high-density structures and their surrounding low-density extended gas.

4.2.2 Leaves vs. isolated structures

Here, we focus on the comparison between isolated structures and leaves—which correspond to the internal dense regions within trunks—based on their adjusted physical properties. Figure 9 displays the ANOVA results and the adjusted distributions for these two structural categories.

As shown in Figure 9(a), leaves and isolated structures exhibit comparable adjusted effective radii, indicating that they form on similar spatial scales. However, the ANOVA reveals that leaves have significantly larger adjusted masses compared to isolated structures (Figure 9(b)). Reflecting this significant difference in mass within similar spatial scales, leaves consequently exhibit significantly higher adjusted volume densities (Figure 9(c)). Furthermore, leaves have significantly lower adjusted virial parameters than isolated structures (Figure 9(d)). These quantitative results robustly demonstrate that, despite forming on similar spatial scales, the interior of hierarchically structured clouds (leaves) achieves a significantly denser and more tightly gravitationally bound environment than isolated structures.

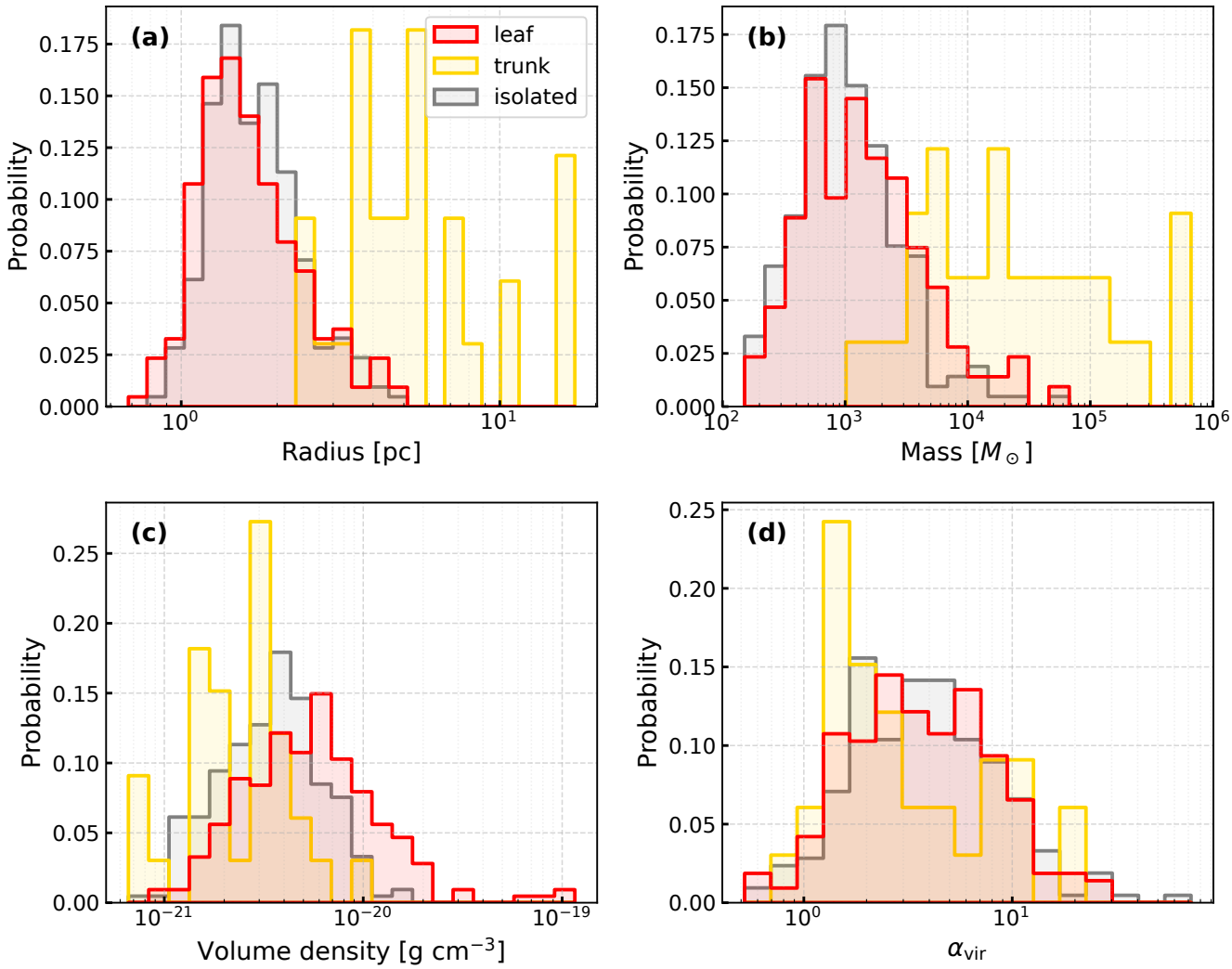

Fig. 7. Probability histograms of the physical properties for the identified structures. The panels show the relative frequencies with respect to (a) effective radius, (b) mass, (c) volume density, and (d) virial parameter ($\alpha_{\rm vir}$). The red, yellow, and grey step-histograms represent leaves, trunks, and isolated structures, respectively. The vertical axis indicates the probability, normalized such that the sum of the bin heights for each structural category equals unity. The horizontal axes are shown in logarithmic scale. Alt text: Four-panel figure of overlaid step histograms comparing the leaf, trunk, and isolated distributions for effective radius, mass, volume density, and virial parameter. In the radius and mass panels the trunk histogram is clearly shifted toward larger values, while the leaf and isolated histograms overlap each other at smaller values; in the volume density and virial parameter panels all three distributions largely overlap.

4.3 Association with YSOs and dense clumps

In this subsection, we investigate the statistical differences in the number of associated YSOs and Hi-GAL clumps between leaves and isolated structures, based on the ANOVA results.

4.3.1 Compare with YSO

Regarding low-mass star formation activity, the background-subtracted number of associated YSOs ($N_{\rm YSO}$) shows no statistically significant difference between leaves and isolated structures, as illustrated in Figure 10(a). To investigate how this low-mass star formation activity varies with specific physical conditions, Figures 11 and 12 present the probability of YSO association and the mean number of contained YSOs, respectively, as a function of the local physical parameters (effective radius, mass, volume density, and virial parameter). As shown in these figures, both values fall well within mutual error bars for both structural categories across all examined physical parameters. These uniform distributions demonstrate that the fundamental rate of low-mass star formation is primarily a local process governed by the properties of the dense gas, exhibiting no significant dependence on the macroscopic hierarchical nature of the host structure.

On the other hand, as shown in Figure 10(b), the adjusted SFE is significantly lower in leaves than in isolated structures. Because the absolute number of YSOs ($N_{\rm YSO}$) is the same in both environments, this lower SFE simply reflects the leaves' much larger gas reservoirs ($M_{\rm gas}$) rather than any reduction in star-forming activity: the leaves are gas-rich relative to their unchanged low-mass stellar content. The physically essential result for low-mass star formation is therefore the invariance of the YSO count itself, on which we focus in the following.

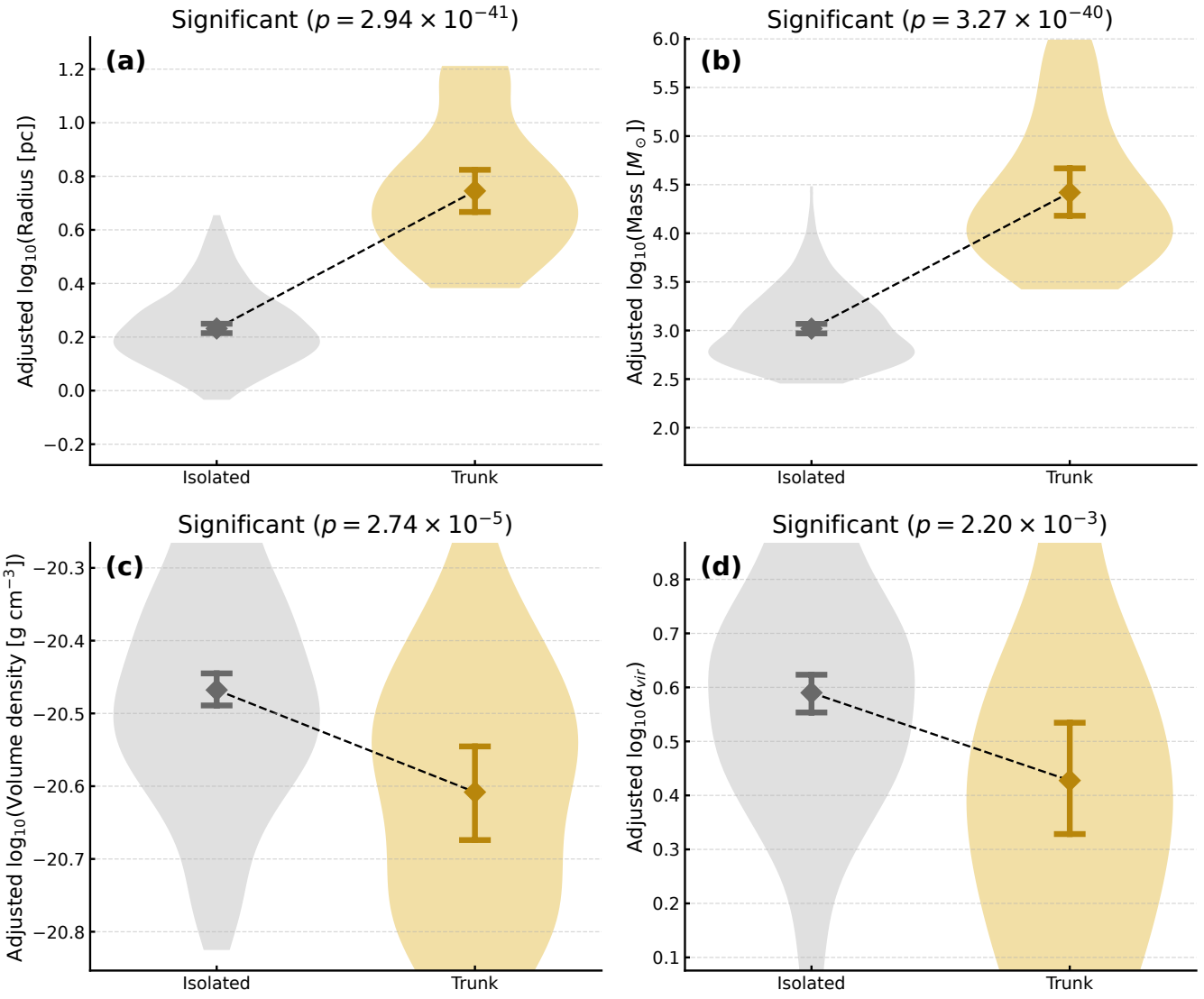

Fig. 8. Comparison of the adjusted physical properties between isolated structures and trunks based on the analysis of variance (ANOVA). The panels show the adjusted values for (a) effective radius, (b) mass, (c) volume density, and (d) virial parameter ($\alpha_{\rm vir}$) in logarithmic scale. The grey and yellow shaded regions show the violin plots for isolated structures and trunks, respectively. The diamond markers indicate the estimated means, and the error bars represent the 95% bootstrap confidence intervals. The dashed line connects the means of the two categories. The p-value of the statistical test is displayed at the top of each panel. Alt text: Four-panel violin plot comparing the adjusted distributions of isolated structures and trunks for effective radius, mass, volume density, and virial parameter. From isolated to trunk, the mean rises in the effective radius and mass panels and falls in the volume density and virial parameter panels, and all four panels report a statistically significant difference between the two categories.

4.3.2 Compare with Hi-GAL clump

In contrast to the low-mass YSOs, the early stages of high-mass star formation traced by Hi-GAL clumps exhibit a distinctly different environmental dependence. As shown in the ANOVA results of Figure 13(a) and (b), leaves contain a significantly higher number of Hi-GAL clumps ($N_{\rm clump}$) and a substantially larger total clump mass ($M_{\rm clump}$) compared to isolated structures. However, when evaluating the Clump Formation Efficiency (CFE), Figure 13(c) reveals that the adjusted CFE shows no statistically significant difference between leaves and isolated structures. Given the relationship $M_{\rm clump} = {\rm CFE} \times M_{\rm gas}$, this constant efficiency implies that the elevated clump formation in leaves is not driven by an enhanced local conversion rate, but is instead a direct consequence of the significantly larger gas reservoirs ($M_{\rm gas}$) available within hierarchical environments.

The adjusted CFE values for both isolated structures and leaves are centered around a high mean value of approximately 70%, with a small fraction of structures even exceeding unity. Previous studies on Galactic molecular clouds (e.g., Eden et al. 2012, 2013) generally reported a much lower CFE typically ranging from a few percent to 10%. However, their evaluated cloud masses are on the order of 10^4–10^5 $M_\odot$, which corresponds to the macroscopic scale of the trunks in our analysis. In contrast, the leaf and isolated structures compared here represent localized, highly condensed environments whose gas masses are roughly an order of magnitude smaller than those of the trunks. Therefore, it is reasonable that our calculated CFE values shift to a significantly higher range. Additionally, for the specific structures where the CFE exceeds 100%, the high optical depth of the ^{13}CO ($J = 1 - 0$) emission in extremely dense regions likely leads to an underestimation

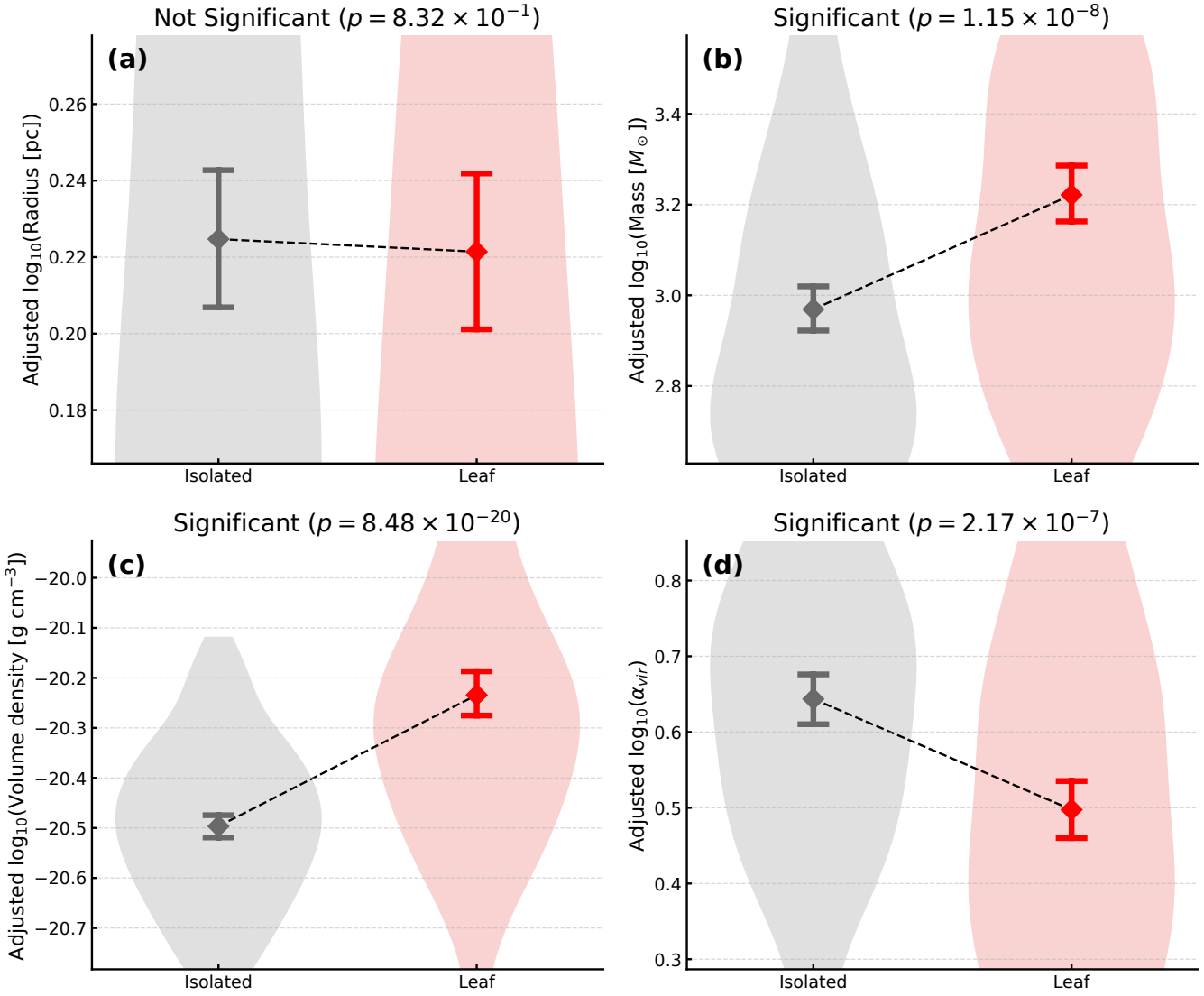

Fig. 9. Same as Figure 8, but for the comparison between isolated structures and leaves. The red shaded regions, diamond markers, and error bars represent leaves. Alt text: Four-panel violin plot comparing the adjusted distributions of isolated structures and leaves for effective radius, mass, volume density, and virial parameter. The effective radius panel shows nearly equal means with no statistically significant difference, while from isolated to leaf the mean rises significantly in the mass and volume density panels and falls significantly in the virial parameter panel.

of the local gas mass ($M_{\rm gas}$), further contributing to these extreme values.

To investigate how this clump formation activity varies with specific physical conditions, Figures 14, 15, and 16 present the probability of Hi-GAL clump association, the number of contained clumps, and the total mass of these clumps, respectively, as a function of the local physical parameters (effective radius, mass, volume density, and virial parameter). As shown in Figure 14, the probability of Hi-GAL clump association for both structures falls well within their mutual error bars across all physical parameters, indicating that the fundamental capability to initiate high-mass star formation depends primarily on local conditions rather than the macroscopic hierarchy. Despite this similar initiation probability, a striking contrast emerges in the absolute quantities under extreme physical conditions. Specifically, at the largest radii, highest masses, and lowest virial parameters, leaves contain both a distinctly larger number of clumps (Figure 15) and a significantly larger total clump mass (Figure 16) than isolated structures, exceeding their mutual error bars.

Integrating these observational results clarifies the causal relationship governing massive clump formation in hierarchical environments. As demonstrated by the physical parameter dependencies, leaves harbor a significantly larger number and total mass of clumps than isolated structures specifically when they possess extreme macroscopic properties: the largest radii, highest masses, and lowest virial parameters. Given that the conversion fraction (CFE) remains constant, acquiring such an enhanced population of clumps mathematically necessitates that the host structure gathers a correspondingly enormous gas reservoir ($M_{\rm gas}$). Therefore, the causal link is clear: it is precisely because these leaves can grow into such massive and tightly gravitationally bound structures—capable of accumulating and retaining vast amounts of gas—that they can achieve clump formation on a scale that significantly exceeds isolated environments. These extreme

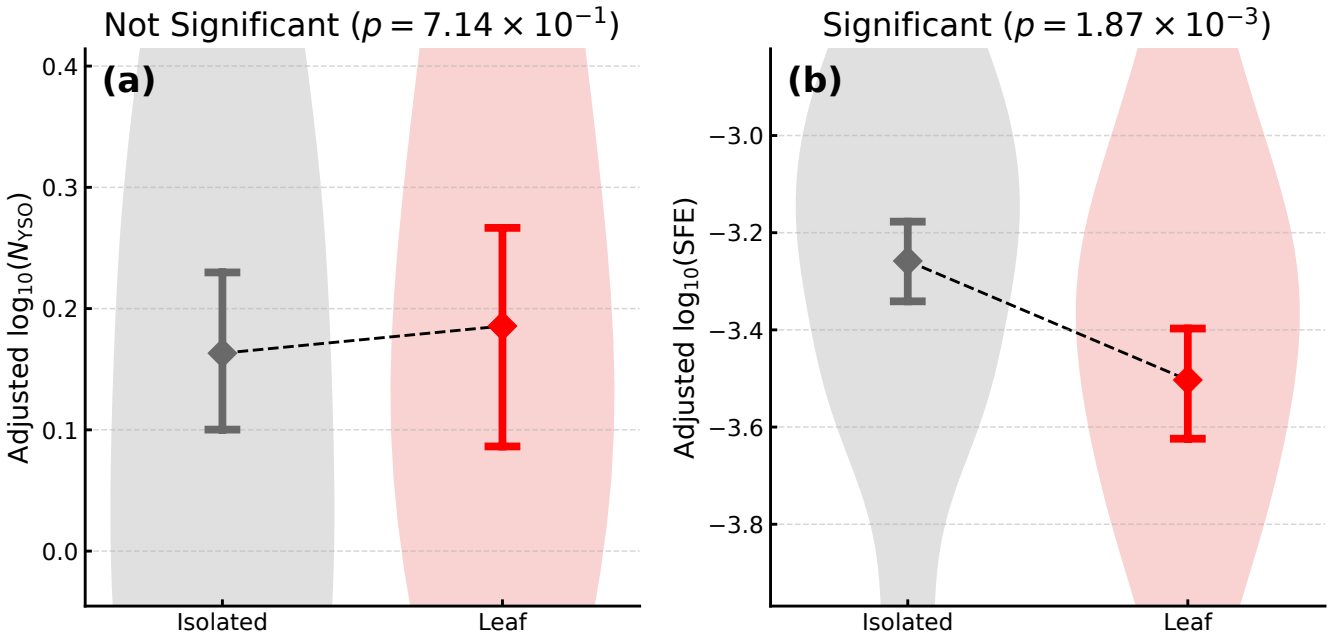

Fig. 10. Comparison of the adjusted (a) number of associated YSOs ($\log_{10} N_{\rm YSO}$) and (b) Star Formation Efficiency ($\log_{10}$ SFE) between isolated structures and leaves based on the ANOVA. The grey and red shaded regions show the violin plots for isolated structures and leaves, respectively. The diamond markers indicate the estimated means, and the error bars represent the 95% bootstrap confidence intervals. The dashed line connects the means of the two categories. The p-value of the statistical test is displayed at the top of each panel. Alt text: Two-panel violin plot comparing the adjusted distributions of isolated structures and leaves for the number of associated young stellar objects and the star formation efficiency. The number of young stellar objects shows nearly equal means with no statistically significant difference, while the star formation efficiency is significantly lower in leaves than in isolated structures.

physical properties strongly suggest that leaves are dynamically growing systems, where continuous mass accumulation prevents gas depletion even when multiple high-mass clumps are actively forming. A detailed discussion on the evolutionary scenario and the specific physical mechanisms enabling this sustained structural growth is presented in Section 5.

5 Discussion

5.1 Hierarchical mass accumulation and mutual interactions

In Section 4.1, the per-region comparison shows that the trunks trace recognizable morphological structures together with their associated internal kinematics: the filamentary morphology of N14, whose oscillatory velocity pattern is attributed to internal contraction, and the hub-filament morphology of W33, whose velocity gradients trace infall along the filaments toward the central hub. Distinct from these morphology-defined cases, the trunks in W51 A and N35 instead mark the sites of cloud–cloud collisions—a dynamical assembly process that does not presuppose any particular morphology—as revealed by their collision-attributed kinematic signatures. In all of these regions, the internal leaves pick out the dense gas concentrations within the trunks. This correspondence suggests that, in these regions, the dendrogram hierarchy traces physically meaningful structures. In Sections 4.2.1 and 4.2.2, the sample-wide statistics show that the trunks are systematically more massive, larger, and more strongly bound (i.e., exhibit lower virial parameters) than isolated structures, and that the leaves, despite spatial scales comparable to isolated structures, are significantly denser and more tightly bound.

We interpret the dense, strongly bound state of the leaves as a consequence of their residing within the massive trunks: the deep gravitational potential of such a reservoir confines the internal substructure—enhancing its boundedness—and feeds it through accretion onto the dense regions and, plausibly, interactions among them, allowing the leaves to grow denser than comparable isolated structures. This interpretation can be grounded physically in the regions of Section 4.1 amenable to a qualitative characterization. Where the internal kinematics of a trunk are resolved, the gas is seen streaming inward toward the dense regions—the oscillatory contraction within the N14 filament and the velocity gradients along the W33 filaments toward the central hub—consistent with the accretion invoked above. These massive reservoirs, with their filamentary and hub-filament morphologies, may in turn arise from large-scale dynamical processes that gather and compress the gas; in W51 A and N35 we capture one such process directly, where the trunks coincide with cloud–cloud collisions. The W51 A configuration also speaks to the second channel: there the leaves are not confined to a single coherent flow but are scattered across the distinct, mutually converging velocity components of the collision (Section 4.1.2), so that as these components are driven together the leaves embedded in them are correspondingly brought into contact, plausibly driving the interactions invoked above—though on a more indirect basis than the inflow signatures behind the accretion channel, since we resolve the leaves on separate converging components but not the interactions themselves. It should be noted that these kinematic correspondences are available only in this small subset of regions and, resting on a static snapshot, cannot by themselves constrain the temporal history of the gas, leaving the same contrasts consistent with a quasi-steady state. We therefore read

this picture as a structural interpretation rather than a measured evolutionary sequence; within that scope, the deep potentials of the massive trunks provide a coherent, physically grounded explanation for the sample-wide finding that their internal leaves are significantly denser and more tightly bound than comparable isolated structures.

To place our proposed scenario in a broader context, the physical origin of the large-scale dynamical events that assemble the trunks warrants consideration at galactic scales. Observational studies of nearby galaxies have demonstrated that spiral arms play a fundamental role in gathering gas and assembling massive giant molecular clouds (e.g., Koda et al. 2009; Hirota et al. 2011). More specifically, recent high-resolution observations of the Local Group galaxy M33 have revealed that the physical environments within these spiral arms actively induce dynamic events, such as filament formation and cloud-cloud collisions (e.g., Tokuda et al. 2020; Kondo et al. 2021). These arm-driven phenomena are reminiscent of the dynamical events invoked in our scenario for assembling the massive trunks. Although a direct connection to our own regions remains to be established, this suggests that environments like spiral arms could provide a natural setting for the large-scale gas assembly we infer.

5.2 Environmental dependence of YSO and clump formation

As presented in Section 4.3.1, the associated $N_{\rm YSO}$ shows no statistically significant difference between leaves and isolated structures. This invariance, independent of the surrounding hierarchical environment, is consistent with the established view that low-mass star formation is a fundamentally local process governed by the properties of the dense gas rather than by macroscopic cloud properties (e.g., Lada 1992; Gao & Solomon 2004; Wu et al. 2005; Lada et al. 2010; Wu et al. 2010). Lada et al. (2010) showed that local star formation is regulated by the total mass of gas exceeding a volume density threshold of $n > 10^4$ cm^{-3}. In our sample, the adjusted mean number density of the leaf structures is $\sim 10^3$ cm^{-3}, about an order of magnitude below this threshold. The invariance of $N_{\rm YSO}$ therefore implies that the mass of dense, star-forming gas above this threshold is comparable between leaves and isolated structures, even though the total gas reservoir ($M_{\rm gas}$) of the leaves is substantially larger; the additional gas in the leaves resides largely at intermediate densities and does not contribute to the present low-mass star formation. For this surplus reservoir to produce a low-mass stellar population proportional to its mass, the leaf gas would have to fragment further into substructures exceeding the critical density. Why such fragmentation does not proceed — and what becomes of the accumulated gas instead — is examined in the remainder of this section.

In contrast to the YSOs, the physical properties of the gas clumps show a clear environmental dependence (Section 4.3.2): the clumps associated with leaves are significantly more numerous and more massive than those in isolated structures. Crucially, this enhancement is observed even though the clump formation efficiency (CFE) is statistically indistinguishable between the two environments. Given the relation $M_{\rm clump} = {\rm CFE} \times M_{\rm gas}$, a constant CFE implies that the enhanced clump content of the leaves follows directly from their larger gas reservoirs ($M_{\rm gas}$), rather than from a higher local efficiency of converting gas into clumps. In isolated structures the total gas mass is intrinsically limited, which caps the clump mass and number attainable at a fixed efficiency; the larger reservoirs of the leaves remove this ceiling. These larger reservoirs are themselves a structural property of the leaves: they reside within the deep gravitational potentials of the macroscopic trunks, which—as the morphological and kinematic correspondences in Section 5.1 suggest—can act as the source of this gas. We stress, however, that our static data constrain only this structural contrast: whether the reservoirs are actively sustained by continuous large-scale inflow and mutual interactions among the leaves, or instead represent a quasi-steady configuration, cannot be determined from a single snapshot.

This contrast between the invariant low-mass population and the enhanced massive-clump content suggests that the characteristic scale of fragmentation may be larger within the leaves: rather than fragmenting into a proportionally larger number of low-mass cores, the accumulated gas appears to be channeled preferentially into massive clumps. Such a shift is the expected signature of accretion-modified fragmentation, in which the continuous mass transport inherent to dynamic environments raises the characteristic fragmentation mass and suppresses small-scale fragmentation (Li 2024). Observationally, super-Jeans fragmentation—dense cores more massive and more widely separated than the thermal Jeans prediction—has been reported in a number of massive star-forming regions (Zhang et al. 2009; Wang et al. 2014; Xu et al. 2023), and a recent triangulation analysis recovers precisely this signature as anticipated by Li (2024) (Li et al. 2025). Such super-Jeans behavior is not universal—other regions are well described by thermal Jeans fragmentation (e.g., Sanhueza et al. 2019; Lu et al. 2020)—but this very dichotomy has been attributed to differences in the local mass-accumulation rate (Li 2024), consistent with the mechanism operating preferentially in the most dynamic, accreting environments such as the leaves embedded within the trunks. Translating this mechanism into a quantitative prediction for our own structures is, however, beyond the reach of our data: the accretion rate that sets the magnitude of the effect cannot be measured from a single-epoch snapshot, and a Jeans-mass estimate built on our observables would in any case be incomplete, capturing only thermal and turbulent support. We therefore keep this argument qualitative. Importantly, the ingredients absent from such a static estimate all act in the same direction: accretion-driven transport (Li 2024), magnetic pressure—amplified by shock compression in dynamic environments such as CCCs (e.g., Inoue & Fukui 2013)—and radiative heating in the densest gas each raise the effective fragmentation mass and further suppress small-scale fragmentation. It is the robustness of this shared directionality, rather than any single quantitative threshold, that makes accretion-modified fragmentation a compelling qualitative explanation for the observed contrast: a low-mass YSO population comparable to that of isolated structures, coexisting with markedly enhanced massive-clump formation.

We caution that the apparent invariance of the YSO counts between the leaves and isolated structures may be partly affected by an observational selection effect. Because the leaf structures trace systematically higher column densities, the completeness of the mid-infrared YSO census within them may be reduced by the increased extinction and the brighter, more structured background that hampers point-source detection in dense regions. This effect acts in a single direction, preferentially suppressing the observed YSO counts in the leaves; the values we report should therefore be treated as lower limits, and we cannot exclude that some enhancement of low-mass star formation in the leaves is masked by incompleteness. Crucially, however, this limitation does not propagate to our central result. The clump enhancement is traced by the Hi-GAL far-infrared and submillimeter dust emission, which

probes deeply embedded material and is essentially insensitive to the extinction and background that limit the mid-infrared YSO census; the pronounced contrast in clump number and mass between the leaves and isolated structures is thus robust against this bias. Accordingly, our conclusions rest primarily on this high-mass clump enhancement, while the low-mass YSO census is best interpreted as providing no positive evidence for a comparable enhancement rather than as firmly excluding one. A completeness-robust characterization of the low-mass population in these dense environments will require future extinction-insensitive observations.

5.3 Physical scenario for massive clump formation in hierarchical clouds

Synthesizing the discussions of hierarchical mass accumulation (Section 5.1) and the environmental dependence of star formation (Section 5.2), the physical processes underlying massive clump formation within hierarchically structured clouds can be summarized as the self-consistent physical scenario illustrated in Figure 17. As established in Section 5.1, the trunks are systematically more extended, more massive, and more deeply gravitationally bound than isolated structures, marking them as the large-scale gas reservoirs of the hierarchy. In the subset of regions amenable to a qualitative characterization, these reservoirs further appear to be assembled by large-scale dynamical processes that gather and compress the gas. In some of these regions, such a process is traced through the resulting morphology, as in filaments and hub–filament systems. In others, it is instead traced through the assembling event itself, of a kind that may give rise to such morphologies, as in cloud–cloud collisions. Within these reservoirs, the embedded leaves are significantly denser and more tightly bound than isolated structures of comparable scale, consistent with their growing by acquiring mass through sustained accretion and mutual interactions (Section 5.1). This continuous mass supply may increase the characteristic fragmentation mass within the leaves, as suggested by numerical studies (e.g., Li 2024; Section 5.2), helping to channel the accumulated gas into massive clumps rather than a proportionally larger population of low-mass stars.

The evidence behind this scenario is structural and comparative. Across the sample, the structures embedded in the hierarchy differ systematically from isolated ones (Section 4.2): the leaves are more massive and more strongly gravitationally bound than isolated structures of the same scale, as are the trunks that host them relative to isolated structures overall. Although the virial parameters we derive remain near or above the nominal threshold for boundedness ($\alpha_{\rm vir} = 1$), so that this is a comparative rather than an absolute statement, the shared direction of these contrasts indicates that, within the hierarchy, self-gravity is relatively more important and the substructure more massive than outside it.

The contrasts we have established bear on the competing frameworks for massive star formation (Section 1), and in particular on the scale at which its gas reservoir is set. In the turbulent-core model (McKee & Tan 2002, 2003), that reservoir is essentially local, confined to a single, self-contained core in approximate virial equilibrium, whereas competitive accretion (Bonnell et al. 2001, 2004), global hierarchical collapse (Vázquez-Semadeni et al. 2009, 2019), and the conveyor-belt view (Padoan et al. 2020) place it on larger scales. Our strongest result bears directly on this distinction: the leaves' enhanced massive-clump content follows from how much gas they contain, not from a higher conversion efficiency (Section 4.2). Because the leaves differ from isolated structures precisely in residing within the macroscopic trunks, this larger reservoir is a property of the hierarchical environment rather than of the local structure alone. The mass available for massive-clump formation therefore reflects a structure's place within the larger hierarchy rather than a fixed, local scale, favoring the larger-scale-reservoir family over the local, core-scale picture of the turbulent-core model. That said, our ~ 1 pc resolution lies above the individual cores on which the turbulent-core model is defined, so this bears on where the gas resides rather than on the internal state of the final cores. Our static measurements, moreover, do not on their own discriminate among the larger-scale-reservoir scenarios, which diverge mainly in whether continuous flows feed the reservoirs and in the order in which the hierarchy assembles—properties of the gas dynamics and history that a single-epoch snapshot cannot recover. We therefore read our results as evidence that the gas available for massive star formation is organized on larger scales rather than confined to a local, core-scale reservoir, broadly in keeping with this family of frameworks, while stopping short of identifying any single one—including the global hierarchical collapse picture with which our proposed sequence is most naturally associated.

Discriminating among these scenarios will require the kinematic and temporal information that our single-epoch analysis cannot provide. Velocity diagnostics across multiple molecular transitions and density-selective tracers would allow the inflow and accretion rates to be measured directly, as has been demonstrated for individual hub–filament systems (Peretto et al. 2013), testing whether continuous flows link the successive scales of the hierarchy. Higher-resolution observations reaching the core scale would let the turbulent-core prediction be tested on its own terms, following the high-resolution fragmentation studies of massive clumps (Sanhueza et al. 2019; Lu et al. 2020). Numerical simulations following the time evolution of trunk-scale collapse (e.g., Vázquez-Semadeni et al. 2019) are needed to establish the temporal ordering our scenario implies and to test whether sustained accretion indeed raises the characteristic fragmentation mass (Li 2024). We leave these directions to future work.

6 Summary

In this study, we conducted a comprehensive statistical analysis of the hierarchical gas structures within 13 Galactic star-forming regions using the FUGIN CO survey data. By applying a non-binary dendrogram algorithm to the three-dimensional position-position-velocity data cubes, we extracted the hierarchical structures and classified them into macroscopic trunks, internal leaves, and isolated structures. For several representative regions amenable to a qualitative characterization, we overlaid the identified structures on the position-position and position-velocity diagrams. There, in some regions the trunks correspond to recognizable morphologies such as filaments and hub-filament systems. In others, they instead trace the kinematic signatures of structure-forming events such as cloud-cloud collisions which may give rise to such morphologies. In all of these regions, the internal leaves pick out the dense gas concentrations within the trunks. Across the full sample, our analysis of the adjusted physical properties revealed that trunks are systematically more extended, more massive, and more tightly gravitationally bound than isolated structures, while the leaves embedded within them achieve significantly higher masses, volume densities, and gravitational binding than isolated structures of comparable spatial scales. Regarding star formation activity, low-mass star formation traced by YSOs showed no significant dependence

on the hierarchical environment, whereas the early stages of high-mass star formation traced by Hi-GAL clumps exhibited a distinctly different trend: leaves contain a significantly higher number of clumps and a much larger total clump mass than isolated structures. Because the clump formation efficiency remains comparable between the two categories, this enhancement follows directly from the substantially larger gas reservoirs available within the leaves rather than from a higher local conversion rate. We interpret these contrasts, together with the inward gas motions seen in the position-velocity diagrams, in terms of a scenario in which the deep gravitational potential of the trunks sustains continuous gas accretion onto the internal leaves and promotes mutual interactions among them, plausibly raising the characteristic fragmentation mass so that the accumulated gas is preferentially channeled into exceptionally massive clumps rather than into a proportionally larger population of low-mass stars. We emphasize, however, that our single-epoch data constrain only these structural contrasts; whether the reservoirs are actively sustained by continuous inflow and mutual interactions, or instead reflect a quasi-steady configuration, cannot be determined from a static snapshot. Taken together, these results indicate that the gas available for massive star formation is organized on scales larger than a single core, reflecting a structure's place within the larger hierarchy rather than a fixed, local reservoir. This is broadly in keeping with the family of frameworks that place the mass reservoir on scales beyond the individual core, although our comparative, single-epoch measurements cannot single out any one of them.

Acknowledgments

N.K. was supported by JSPS KAKENHI Grant Number 25H00661. This publication makes use of data from FUGIN, FOREST Unbiased Galactic plane Imaging survey with the Nobeyama 45-m telescope, a legacy project in the Nobeyama 45-m radio telescope. This work made use of Astropy:[1] a community-developed core Python package and an ecosystem of tools and resources for astronomy (Astropy Collaboration et al. 2013, 2018, 2022). This research made use of astrodendro, a Python package to compute dendrograms of Astronomical data (http://www.dendrograms.org/). This research made use of the SPICY catalog (Kuhn et al. 2021) (doi:10.26131/IRSA556) and the Herschel Hi-GAL clump catalog (Elia et al. 2021) (doi:10.26131/IRSA571). In addition, the authors utilized OpenAI's ChatGPT, Google's Gemini, and Anthropic's Claude for coding assistance and English language refinement; however, the final manuscript was reviewed and approved by the authors.

Appendix. Details of the statistical modeling and Type II ANOVA

In this Appendix, we provide the mathematical details of the statistical modeling and analysis of variance (ANOVA) used in Section 4.2. The primary objective of this analysis is to statistically isolate and evaluate the pure differences in physical properties arising from the different hierarchical gas structures (e.g., leaf and isolated), while strictly controlling for the inherent environmental variance across the 13 distinct observed regions. Below, we first formulate the linear model and extend it to a matrix representation, followed by the procedure for parameter estimation using ordinary least squares (OLS). Furthermore, we explicitly demonstrate the computational logic of Type II ANOVA, which accommodates unbalanced sample sizes, using the matrix formulation of a reduced model. Finally, we explain the theoretical background of the adjusted values used for visualization.

The base-10 logarithmic value of a given physical property y_i for each observed data point i ($i = 1, \ldots, n$) can be modeled as a linear combination of the global baseline intercept μ, the environmental bias due to the region $\alpha_{\mathrm{region}(i)}$, the main effect of the hierarchical structure $\beta_{\mathrm{structure}(i)}$, and the residual error representing individual variance ϵ_i, expressed as follows:

$$y_i = \mu + \alpha_{\mathrm{region}(i)} + \beta_{\mathrm{structure}(i)} + \epsilon_i. \tag{9}$$

To solve this computationally, the categorical variables for the region (13 categories) and structure (2 categories) are converted into dummy variables that take values of 0 or 1. To prevent multicollinearity, specific region and structure categories (e.g., isolated) are set as the reference categories, and their corresponding dummy variables are omitted, leaving 12 dummy variables for the regions ($x_\alpha^{(1)} \ldots x_\alpha^{(12)}$) and 1 dummy variable for the structure (x_β) to be considered. Consequently, the system of equations for the entire dataset can be explicitly written down in the following matrix form:

$$\begin{pmatrix} y_1 \\ y_2 \\ \vdots \\ y_n \end{pmatrix} = \begin{pmatrix} 1 & x_{\alpha,1}^{(1)} & \cdots & x_{\alpha,1}^{(12)} & x_{\beta,1} \\ 1 & x_{\alpha,2}^{(1)} & \cdots & x_{\alpha,2}^{(12)} & x_{\beta,2} \\ \vdots & \vdots & \ddots & \vdots & \vdots \\ 1 & x_{\alpha,n}^{(1)} & \cdots & x_{\alpha,n}^{(12)} & x_{\beta,n} \end{pmatrix} \begin{pmatrix} \mu \\ \alpha^{(1)} \\ \vdots \\ \alpha^{(12)} \\ \beta \end{pmatrix} + \begin{pmatrix} \epsilon_1 \\ \epsilon_2 \\ \vdots \\ \epsilon_n \end{pmatrix}. \tag{10}$$

We define this simplified expression as the equation of the full model,

$$\mathbf{Y} = \mathbf{X}\boldsymbol{\theta} + \boldsymbol{\epsilon}. \tag{11}$$

Here, $\mathbf{Y}$ is the observation vector, $\mathbf{X}$ is the design matrix of the full model, $\boldsymbol{\theta}$ is the parameter vector to be estimated, and $\boldsymbol{\epsilon}$ is the residual vector. The optimal value $\hat{\boldsymbol{\theta}}$ of the parameter vector $\boldsymbol{\theta}$ is estimated using ordinary least squares (OLS). OLS is an optimization problem that minimizes the sum of squared errors (SSE) unexplained by the model, which is formulated as follows:

$$SSE_{\mathrm{full}} = \sum_{i=1}^{n} \epsilon_i^2 = (\mathbf{Y} - \mathbf{X}\hat{\boldsymbol{\theta}})^T (\mathbf{Y} - \mathbf{X}\hat{\boldsymbol{\theta}}). \tag{12}$$

By taking the partial derivative of this objective function with respect to $\boldsymbol{\theta}$ and setting it to zero, the normal equations are obtained, and their analytical solution is uniquely derived as follows:

$$\hat{\boldsymbol{\theta}} = (\mathbf{X}^T\mathbf{X})^{-1}\mathbf{X}^T\mathbf{Y}. \tag{13}$$

Through this computation, the intrinsic bias of each region $\hat{\alpha}$ and the main effect of the structural difference $\hat{\beta}$ that best fit the entire dataset are estimated simultaneously.

To verify the statistical significance of the structural differences (β), we employed Type II ANOVA in this study. Because observational data inherently constitute an unbalanced design where the sample size of each structure varies significantly across regions, Type I ANOVA, in which the partitioning of the sum of squares depends on the order of variable entry, is inappropriate. Type II ANOVA evaluates how much the structural factor independently reduces the residual error, after fully accounting for the effects of

[1] http://www.astropy.org

other factors (i.e., regions). For this purpose, a reduced model is constructed by completely excluding the structural dummy variable (the last column) from the design matrix $\mathbf{X}$ of the full model, formulated as follows:

$$\begin{pmatrix} y_1 \\ y_2 \\ \vdots \\ y_n \end{pmatrix} = \begin{pmatrix} 1 & x_{\alpha,1}^{(1)} & \dots & x_{\alpha,1}^{(12)} \\ 1 & x_{\alpha,2}^{(1)} & \dots & x_{\alpha,2}^{(12)} \\ \vdots & \vdots & \ddots & \vdots \\ 1 & x_{\alpha,n}^{(1)} & \dots & x_{\alpha,n}^{(12)} \end{pmatrix} \begin{pmatrix} \mu' \\ \alpha'^{(1)} \\ \vdots \\ \alpha'^{(12)} \end{pmatrix} + \begin{pmatrix} \epsilon'_1 \\ \epsilon'_2 \\ \vdots \\ \epsilon'_n \end{pmatrix}. \quad (14)$$

By redefining the matrices and vectors, the reduced model can be formulated simply as follows:

$$\mathbf{Y} = \mathbf{X}'\boldsymbol{\theta}' + \boldsymbol{\epsilon}'. \quad (15)$$

By applying OLS again to this reduced model, we calculate the sum of squared errors when ignoring the structure, denoted as SSE_{reduced}, which is given by:

$$SSE_{\mathrm{reduced}} = \sum_{i=1}^{n} (\epsilon'_i)^2. \quad (16)$$

The variance (sum of squares) purely explained by the structural differences, SS_β, is strictly defined as the difference in the errors between these two models, which is given by the following equation:

$$SS_\beta = SSE_{\mathrm{reduced}} - SSE_{\mathrm{full}}. \quad (17)$$

Next, these sums of squares are divided by their respective degrees of freedom (df) to normalize them into mean squares (MS), which represent the variance per degree of freedom independent of the number of categories or sample sizes. The degree of freedom allocated to the structural differences, df_β, is the number of structural categories minus one (i.e., $\mathrm{df}_\beta = 1$ for the two categories in this analysis), and the residual degrees of freedom, df_ϵ, is the total number of data points n minus the total number of parameters estimated in the full model. Consequently, the mean square for the structure, MS_β, and the mean square for the residuals, MS_ϵ, are calculated as follows:

$$MS_\beta = \frac{SS_\beta}{\mathrm{df}_\beta}, \quad MS_\epsilon = \frac{SSE_{\mathrm{full}}}{\mathrm{df}_\epsilon}. \quad (18)$$

Then, the test statistic F, which indicates how dominant the pure effect (signal) of the structural differences is over the natural variance (noise) unexplained by the model, is derived as the ratio of these two mean squares, formulated as:

$$F = \frac{MS_\beta}{MS_\epsilon}. \quad (19)$$

Assuming the null hypothesis (H_0: there is no difference in physical properties due to structure, i.e., $\beta = 0$) is true, this test statistic F follows an F-distribution with degrees of freedom $(\mathrm{df}_\beta, \mathrm{df}_\epsilon)$. Finally, by comparing the calculated F-value with the probability density function of this F-distribution, we calculate the p-value, which represents the probability that the observed data (or a more extreme difference) would occur by chance. In this study, by confirming that this p-value falls below the pre-determined significance level ($\alpha = 0.05$), we mathematically demonstrate the significant main effect of the structure ($\beta_{\mathrm{structure}}$) under conditions where the influence of the environmental bias (α_{region}) is completely controlled.

Finally, to visually demonstrate the statistical evaluations of the ANOVA described above, we use adjusted values rather than raw observational data in the visualizations, such as the violin plots presented in Section 4.2. These adjusted values are calculated using the parameter vector $\hat{\boldsymbol{\theta}}$ strictly estimated by the OLS of the full model. Specifically, the estimated environmental bias of the corresponding region, $\hat{\alpha}_{\mathrm{region}(i)}$, is subtracted from each raw data point y_i, which is formulated as follows:

$$y_{\mathrm{adj},i} = y_i - \hat{\alpha}_{\mathrm{region}(i)} = \hat{\mu} + \hat{\beta}_{\mathrm{structure}(i)} + \hat{\epsilon}_i. \quad (20)$$

Through this subtraction, the environmental baseline differences across the 13 regions are completely eliminated. It should be noted that, to maintain an intuitive physical scale on the y-axis, the global mean of the raw data is added back to these adjusted values during the final plotting process. Consequently, the differences in the distributions appearing on the graphs purely reflect the structural differences ($\hat{\beta}$) and the natural variance ($\hat{\epsilon}$), ensuring that the visual representations are perfectly consistent with the mathematical conclusions drawn from the Type II ANOVA.

References

Anderson, L. D., & Bania, T. M. 2009, ApJ, 690, 706
André, P., Di Francesco, J., Ward-Thompson, D., Inutsuka, S.-I., Pudritz, R. E., & Pineda, J. E. 2014, in Protostars and Planets VI, ed. H. Beuther, R. S. Klessen, C. P. Dullemond, & T. Henning, 27–51
André, P., et al. 2010, A&A, 518, L102
Astropy Collaboration, et al. 2013, A&A, 558, A33
Astropy Collaboration, et al. 2018, AJ, 156, 123
Astropy Collaboration, et al. 2022, ApJ, 935, 167
Ballesteros-Paredes, J., Vázquez-Semadeni, E., Gazol, A., Hartmann, L. W., Heitsch, F., & Colín, P. 2011, MNRAS, 416, 1436
Beltrán, M. T., et al. 2013, A&A, 552, A123
Bertoldi, F., & McKee, C. F. 1992, ApJ, 395, 140
Bhadari, N. K., Dewangan, L. K., Ojha, D. K., Pirogov, L. E., & Maity, A. K. 2022, ApJ, 930, 169
Bonatto, C., Santos, Jr., J. F. C., & Bica, E. 2006, A&A, 445, 567
Bonnell, I. A., Bate, M. R., Clarke, C. J., & Pringle, J. E. 2001, MNRAS, 323, 785
Bonnell, I. A., Vine, S. G., & Bate, M. R. 2004, MNRAS, 349, 735
CASA Team, et al. 2022, PASP, 134, 114501
Chibueze, J. O., et al. 2016, MNRAS, 460, 1839
Dewangan, L. K., Baug, T., Pirogov, L. E., & Ojha, D. K. 2020, ApJ, 898, 41
Dickman, R. L. 1978, ApJS, 37, 407
Dufton, P. L., et al. 2006, A&A, 457, 265
Eden, D. J., Moore, T. J. T., Morgan, L. K., Thompson, M. A., & Urquhart, J. S. 2013, MNRAS, 431, 1587
Eden, D. J., Moore, T. J. T., Plume, R., & Morgan, L. K. 2012, MNRAS, 422, 3178
Elia, D., et al. 2017, MNRAS, 471, 100
Elia, D., et al. 2021, MNRAS, 504, 2742
Evans, II, N. J., et al. 2009, ApJS, 181, 321
Fujita, S., et al. 2019, ApJ, 872, 49
Fujita, S., et al. 2021, PASJ, 73, S172
Fukui, Y., Habe, A., Inoue, T., Enokiya, R., & Tachihara, K. 2021, PASJ, 73, S1
Fukui, Y., et al. 2014, ApJ, 780, 36
Fukui, Y., et al. 2016, ApJ, 820, 26
Furukawa, N., Dawson, J. R., Ohama, A., Kawamura, A., Mizuno, N., Onishi, T., & Fukui, Y. 2009, ApJL, 696, L115
Gao, Y., & Solomon, P. M. 2004, ApJ, 606, 271
Goldsmith, P. F., Heyer, M., Narayanan, G., Snell, R., Li, D., & Brunt, C. 2008, ApJ, 680, 428
Goodman, A. A., Rosolowsky, E. W., Borkin, M. A., Foster, J. B., Halle, M., Kauffmann, J., & Pineda, J. E. 2009, Nature, 457, 63
Guarcello, M. G., Prisinzano, L., Micela, G., Damiani, F., Peres, G., & Sciortino, S. 2007, A&A, 462, 245

Habe, A., & Ohta, K. 1992, PASJ, 44, 203
Hasegawa, T., Sato, F., Whiteoak, J. B., & Miyawaki, R. 1994, ApJL, 429, L77
He, S., et al. 2026, ApJ, 996, 62
Hirota, A., Kuno, N., Sato, N., Nakanishi, H., Tosaki, T., & Sorai, K. 2011, ApJ, 737, 40
Houlahan, P., & Scalo, J. 1992, ApJ, 393, 172
Immer, K., Reid, M. J., Menten, K. M., Brunthaler, A., & Dame, T. M. 2013, A&A, 553, A117
Inoue, T., & Fukui, Y. 2013, ApJL, 774, L31
Inoue, T., Hennebelle, P., Fukui, Y., Matsumoto, T., Iwasaki, K., & Inutsuka, S.-i. 2018, PASJ, 70, S53
Kamazaki, T., et al. 2012, PASJ, 64, 29
Kashiwagi, R., Iwasaki, K., & Tomisaka, K. 2023, ApJ, 954, 129
Kashiwagi, R., Iwasaki, K., & Tomisaka, K. 2024, ApJ, 974, 265
Kerton, C. R., Arvidsson, K., & Alexander, M. J. 2013, AJ, 145, 78
Koda, J., et al. 2009, ApJL, 700, L132
Kondo, H., et al. 2021, ApJ, 912, 66
Kuhn, M. A., de Souza, R. S., Krone-Martins, A., Castro-Ginard, A., Ishida, E. E. O., Povich, M. S., Hillenbrand, L. A., & COIN Collaboration. 2021, ApJS, 254, 33
Kumar, M. S. N., Palmeirim, P., Arzoumanian, D., & Inutsuka, S. I. 2020, A&A, 642, A87
Kuno, N., et al. 2011, in 2011 XXXth URSI General Assembly and Scientific Symposium (IEEE), 1035
Lada, C. J., Lombardi, M., & Alves, J. F. 2010, ApJ, 724, 687
Lada, E. A. 1992, ApJL, 393, L25
Li, C., Wang, H., Zhang, M., Ma, Y., Fang, M., & Yang, J. 2018, ApJS, 238, 10
Li, G.-X. 2024, MNRAS, 528, 7333
Li, G.-X., Zhao, M., & Lu, X. 2025, MNRAS, 541, 3869
Liu, X.-L., Xu, J.-L., Wang, J.-J., Yu, N.-P., Zhang, C.-P., Li, N., & Zhang, G.-Y. 2021, A&A, 646, A137
Lu, X., Cheng, Y., Ginsburg, A., Longmore, S. N., Kruijssen, J. M. D., Battersby, C., Zhang, Q., & Walker, D. L. 2020, ApJL, 894, L14
McKee, C. F., & Tan, J. C. 2002, Nature, 416, 59
McKee, C. F., & Tan, J. C. 2003, ApJ, 585, 850
Minamidani, T., et al. 2016, in Society of Photo-Optical Instrumentation Engineers (SPIE) Conference Series, Vol. 9914, Millimeter, Submillimeter, and Far-Infrared Detectors and Instrumentation for Astronomy VIII, ed. W. S. Holland & J. Zmuidzinas, 99141Z
Molinari, S., et al. 2016, A&A, 591, A149
Motte, F., Bontemps, S., & Louvet, F. 2018, ARA&A, 56, 41
Myers, P. C. 2009, ApJ, 700, 1609
Nakamura, F., et al. 2014, ApJL, 791, L23
Nozaki, S., & Inutsuka, S.-i. 2026, ApJL, 1000, L31
Ortega, M. E., Paron, S., Giacani, E., Rubio, M., & Dubner, G. 2013, A&A, 556, A105
Padoan, P., Pan, L., Juvela, M., Haugbølle, T., & Nordlund, Å. 2020, ApJ, 900, 82
Peretto, N., et al. 2013, A&A, 555, A112
Rosolowsky, E. W., Pineda, J. E., Kauffmann, J., & Goodman, A. A. 2008, ApJ, 679, 1338
Sanhueza, P., et al. 2019, ApJ, 886, 102
Sato, M., Reid, M. J., Brunthaler, A., & Menten, K. M. 2010, ApJ, 720, 1055
Schneider, N., et al. 2012, A&A, 540, L11
Schneider, S., & Elmegreen, B. G. 1979, ApJS, 41, 87
Shen, R., Ma, Y., Wang, H., He, S., & Zhang, M. 2024, ApJ, 971, 14
Sofue, Y. 2023, MNRAS, 525, 4540
Storm, S., et al. 2014, ApJ, 794, 165
Tokuda, K., et al. 2020, ApJ, 896, 36
Torii, K., et al. 2018, PASJ, 70, S51
Torii, K., et al. 2021, PASJ, 73, S368
Umemoto, T., et al. 2017, PASJ, 69, 78
Urquhart, J. S., et al. 2018, MNRAS, 473, 1059
Vázquez-Semadeni, E., Gómez, G. C., Jappsen, A.-K., Ballesteros-Paredes, J., & Klessen, R. S. 2009, ApJ, 707, 1023
Vázquez-Semadeni, E., Palau, A., Ballesteros-Paredes, J., Gómez, G. C., & Zamora-Avilés, M. 2019, MNRAS, 490, 3061
Wang, K., et al. 2014, MNRAS, 439, 3275
Wu, J., Evans, II, N. J., Gao, Y., Solomon, P. M., Shirley, Y. L., & Vanden Bout, P. A. 2005, ApJL, 635, L173
Wu, J., Evans, II, N. J., Shirley, Y. L., & Knez, C. 2010, ApJS, 188, 313
Xu, F.-W., et al. 2023, MNRAS, 520, 3259
Zhang, B., Reid, M. J., Menten, K. M., Zheng, X. W., Brunthaler, A., Dame, T. M., & Xu, Y. 2013, ApJ, 775, 79
Zhang, B., et al. 2014, ApJ, 781, 89
Zhang, Q., Wang, Y., Pillai, T., & Rathborne, J. 2009, ApJ, 696, 268

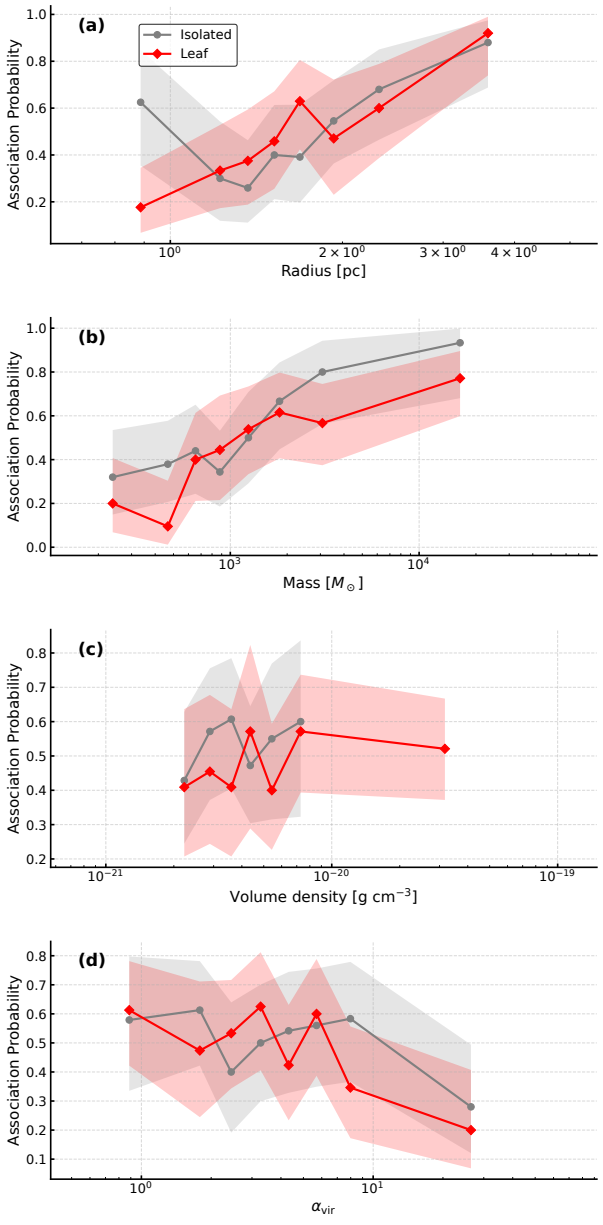

Fig. 11. Association probabilities of YSOs as a function of the local physical properties. The panels show the probabilities against (a) effective radius, (b) mass, (c) volume density, and (d) virial parameter ($\alpha_{\rm vir}$). The red diamonds and grey circles represent leaves and isolated structures, respectively. The shaded regions indicate the 95% Clopper-Pearson exact confidence intervals for the probabilities. To ensure statistical reliability, data points for bins containing fewer than 5 sources are excluded from the plots. The horizontal axes are shown in logarithmic scale. Alt text: Four-panel figure plotting the association probability of young stellar objects for leaf and isolated structures against effective radius, mass, volume density, and virial parameter, each series shown with a confidence band. In every panel the leaf and isolated series track each other with overlapping confidence bands, showing no separation between the two categories at any value of the physical parameters.

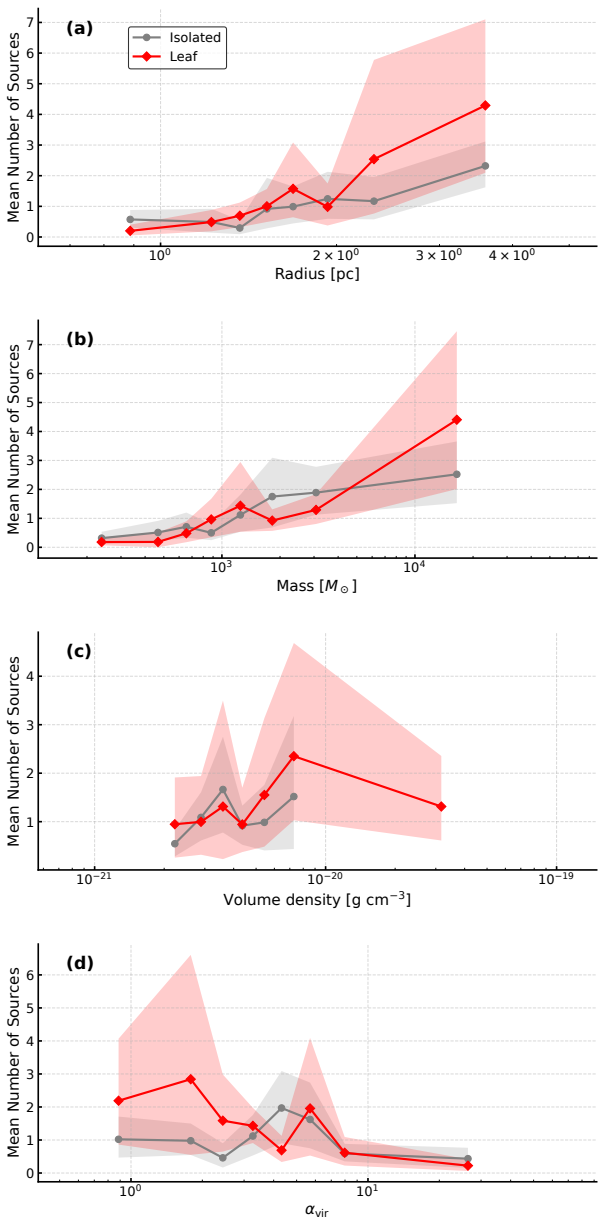

Fig. 12. Mean number of associated YSOs as a function of the local physical properties. The panels show the mean numbers against (a) effective radius, (b) mass, (c) volume density, and (d) virial parameter ($\alpha_{\rm vir}$). The red diamonds and grey circles represent leaves and isolated structures, respectively. The shaded regions indicate the 95% bootstrap confidence intervals. To ensure statistical reliability, data points for bins containing fewer than 5 sources are excluded from the plots. The horizontal axes are shown in logarithmic scale. Alt text: Four-panel figure plotting the mean number of associated young stellar objects for leaf and isolated structures against effective radius, mass, volume density, and virial parameter, each series shown with a confidence band. In every panel the leaf and isolated series track each other with overlapping confidence bands, showing no separation between the two categories.

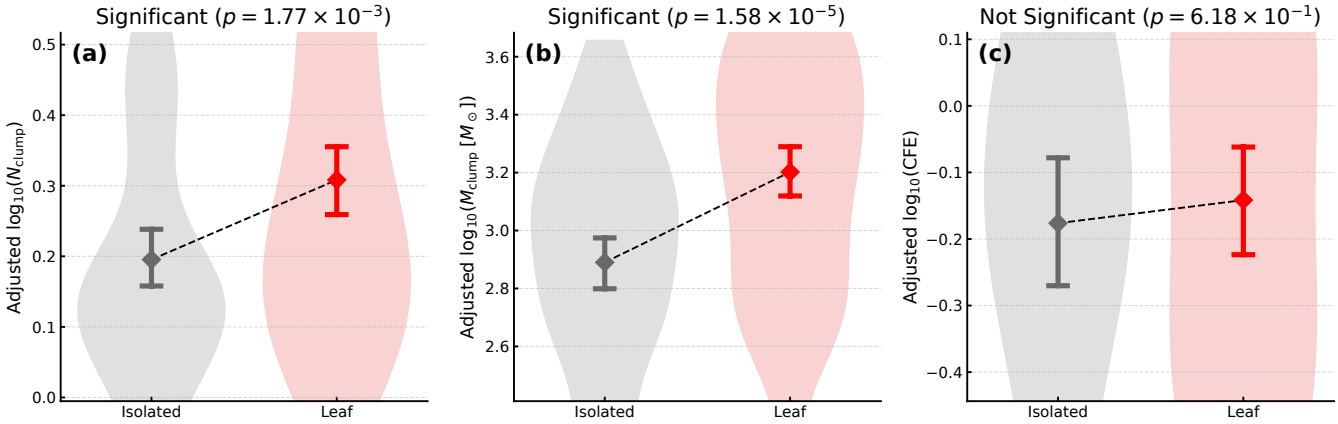

Fig. 13. Same as Figure 10, but for the adjusted (a) number of associated Hi-GAL clumps ($\log_{10} N_{\rm clump}$), (b) total mass of associated Hi-GAL clumps ($\log_{10} M_{\rm clump}$) and (c) Clump Formation Efficiency ($\log_{10}$ CFE). Alt text: Three-panel violin plot comparing the adjusted distributions of isolated structures and leaves for the number of associated Hi-GAL clumps, their total mass, and the clump formation efficiency. The number and total mass of clumps are both significantly higher in leaves than in isolated structures, while the clump formation efficiency shows nearly equal means with no statistically significant difference.

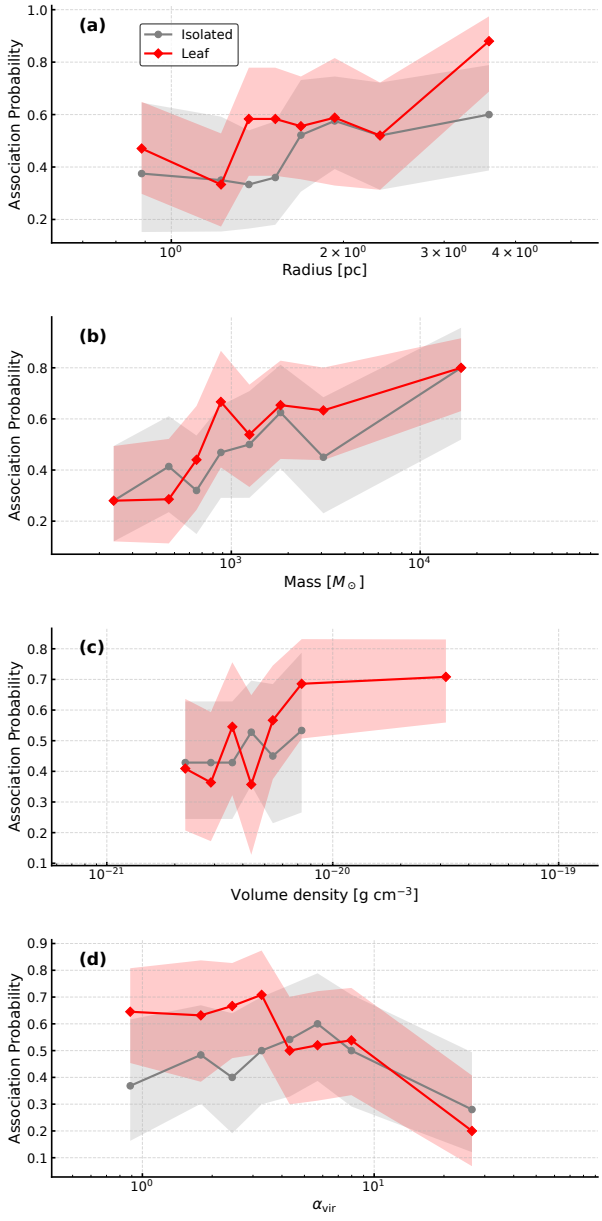

Fig. 14. Same as Figure 11, but for the association probabilities of Hi-GAL clumps. Alt text: Four-panel figure plotting the association probability of Hi-GAL clumps for leaf and isolated structures against effective radius, mass, volume density, and virial parameter, each series shown with a confidence band. In every panel the leaf and isolated series track each other with overlapping confidence bands, showing no separation between the two categories.

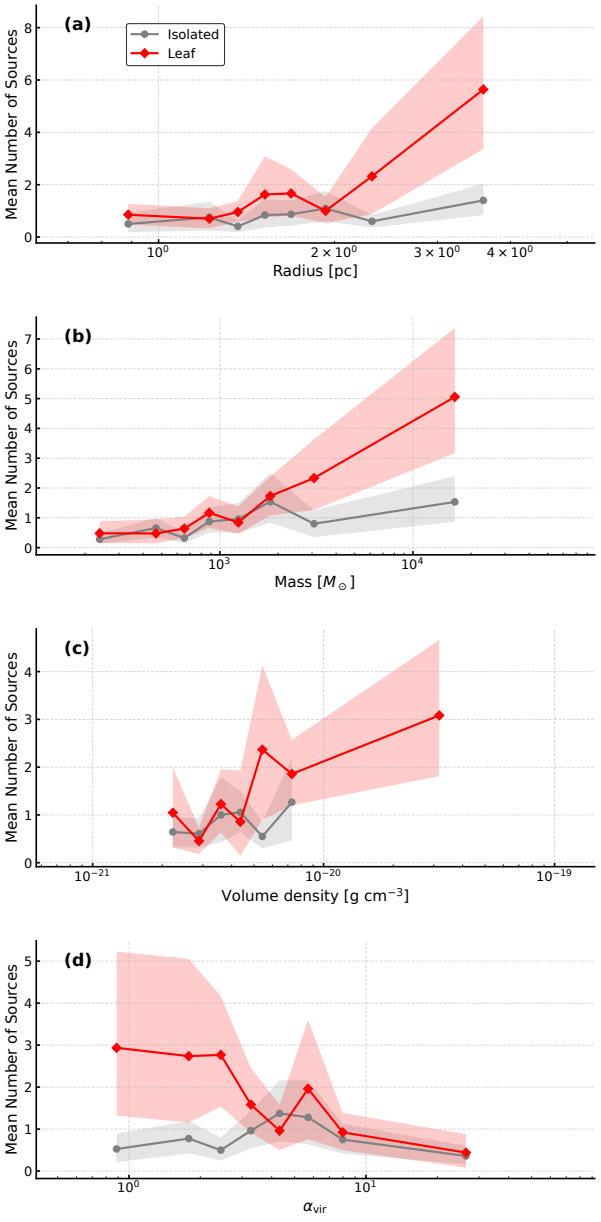

Fig. 15. Same as Figure 12, but for the mean number of associated Hi-GAL clumps. Alt text: Four-panel figure plotting the mean number of associated Hi-GAL clumps for leaf and isolated structures against effective radius, mass, volume density, and virial parameter, each series shown with a confidence band. The two series largely overlap, but at the largest radii, highest masses, and lowest virial parameters the leaf series exceeds the isolated series beyond their error bars.

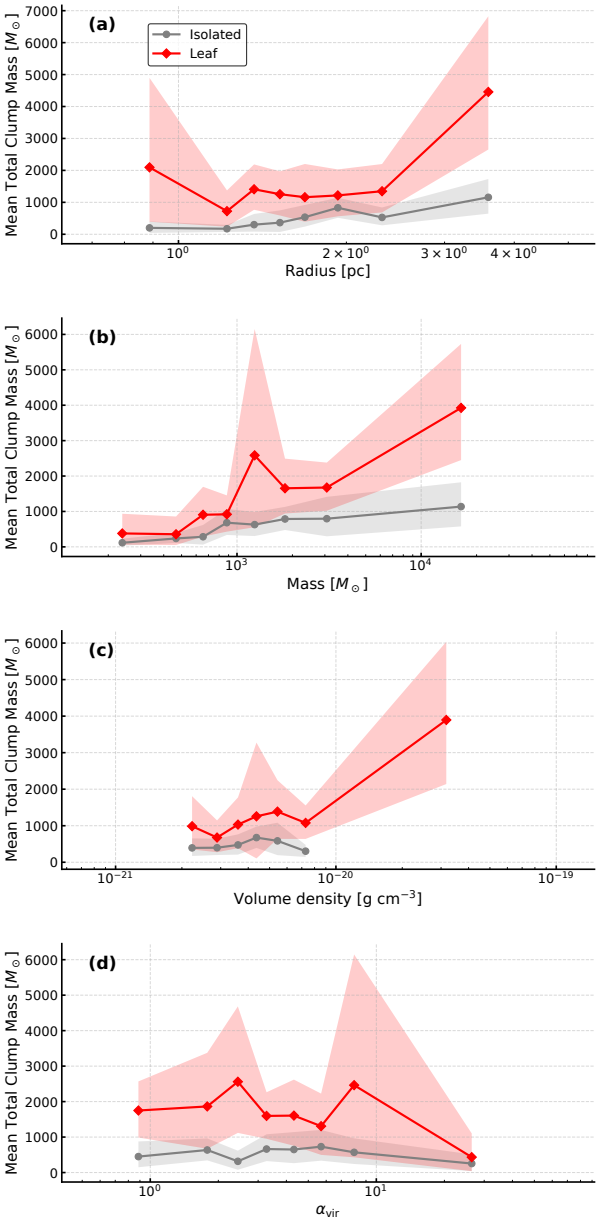

Fig. 16. Same as Figure 12, but for the mean total mass of Hi-GAL clumps. Alt text: Four-panel figure plotting the mean total mass of associated Hi-GAL clumps for leaf and isolated structures against effective radius, mass, volume density, and virial parameter, each series shown with a confidence band. The two series largely overlap, but at the largest radii, highest masses, and lowest virial parameters the leaf series exceeds the isolated series beyond their error bars.

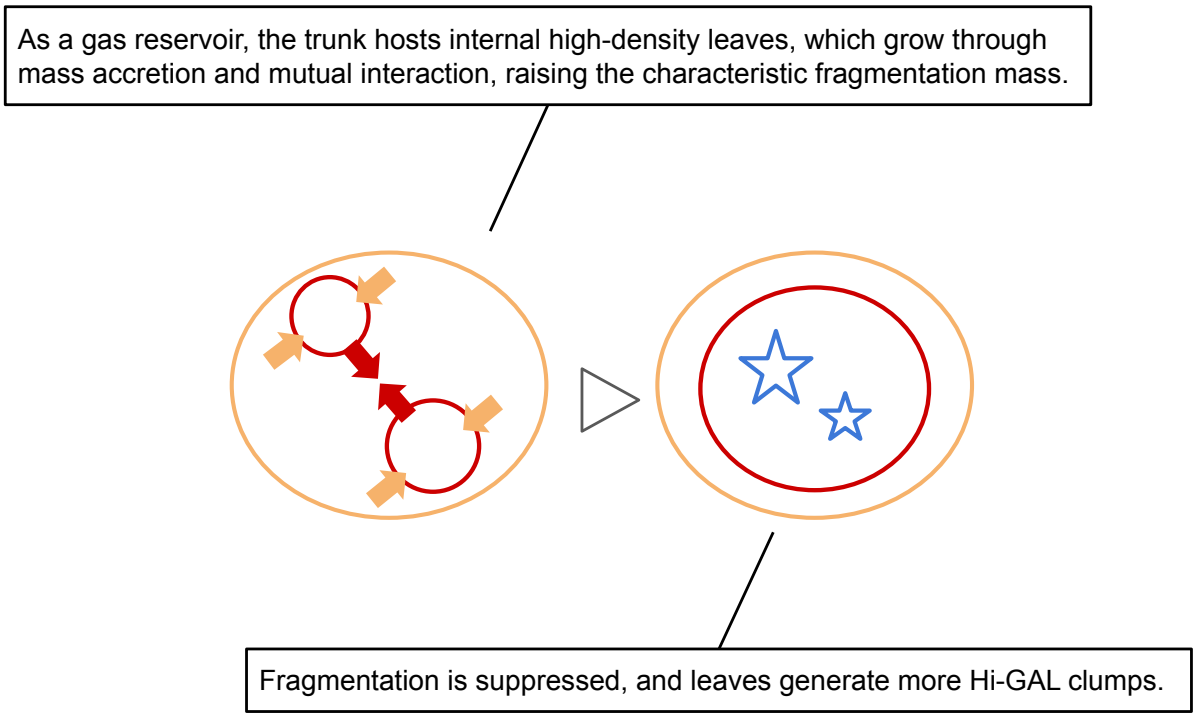

Fig. 17. Schematic of the proposed scenario for massive clump formation within structured molecular clouds. The orange ellipse represents a trunk and the red circles the leaves embedded within it; orange arrows denote gas inflow (accretion) onto the leaves, red arrows mutual interactions and mergers among them, and blue stars the Hi-GAL clumps. Left: acting as a massive, gravitationally bound gas reservoir, the trunk hosts internal high-density leaves that grow through sustained accretion and mutual interaction, raising the characteristic fragmentation mass. Right: this elevated mass scale suppresses fragmentation into low-mass cores, so the accumulated gas is channeled into the formation of numerous massive clumps. Alt text: Two-stage schematic read left to right. Left: an ellipse (trunk) encloses two smaller circles (leaves), with inward arrows feeding the leaves and arrows linking the leaves to each other. Right: the same trunk with the leaves now marked by star symbols representing the Hi-GAL clumps.